

<https://doi.org/10.14379/iodp.proc.381.101.2019>



Contents

1	Abstract
2	Introduction
2	Background
7	Objectives
8	Operational strategy
9	Principal results
20	Preliminary scientific assessment
22	References

Expedition 381 summary¹

L.C. McNeill, D.J. Shillington, G.D.O. Carter, J.D. Everest, E. Le Ber, R.E.Ll. Collier, A. Cvetkoska, G. De Gelder, P. Diz, M.-L. Doan, M. Ford, R.L. Gawthorpe, M. Geraga, J. Gillespie, R. Hemelsdaël, E. Herrero-Bervera, M. Ismaiel, L. Janikian, K. Kouli, S. Li, M.L. Machlus, M. Maffione, C. Mahoney, G. Michas, C. Miller, C.W. Nixon, S.A. Oflaz, A.P. Omale, K. Panagiotopoulos, S. Pechlivanidou, M.P. Phillips, S. Sauer, J. Seguin, S. Sergiou, and N.V. Zakharova²

Keywords: International Ocean Discovery Program, IODP, *D/V Fugro Synergy*, mission-specific platform, Expedition 381, Site M0078, Site M0079, Site M0080, Corinth rift, Gulf of Corinth, Alkyonides Gulf, Eastern Mediterranean Sea, Aegean Sea, continental rifting, extension, active rift, normal fault, earthquake, horst, fault growth, rift development, synrift stratigraphy, drainage evolution, surface processes, basin paleoenvironment, glacio-eustatic cycles, sea level, semi-isolated basin, marine basin, lacustrine, sediment flux, Quaternary, Pliocene, Miocene, carbon cycling, nutrient preservation, marine isotope stage

Abstract

The primary objective of International Ocean Discovery Program Expedition 381 was to retrieve a record of early continental rifting and basin evolution from the Corinth rift, central Greece. Continental rifting is fundamental for the formation of ocean basins, and active rift zones are dynamic regions of high geohazard potential. However, the detailed spatial and temporal evolution of a complete rift system needed to understand rift development from the fault to plate scale is poorly resolved. In the active Corinth rift, deformation rates are high, the recent synrift succession is preserved and complete offshore, and earlier rift phases are preserved onshore. Additionally, a dense seismic database provides high-resolution imaging of the fault network and seismic stratigraphy around the basin. As the basin has subsided, its depositional environment has been affected by fluctuating global sea level and its absolute position relative to sea level, and the basin sediments record this changing environment through time. In Corinth, we can therefore achieve an unprecedented precision of timing and spatial complexity of rift-fault system development, rift-controlled drainage system evolution, and basin fill in the first few million years of rift history. The following are the expedition themes:

- High-resolution fault slip and rift evolution history,
- Surface processes in active rifts,
- High-resolution late Quaternary Eastern Mediterranean paleoclimate and paleoenvironment of a developing rift basin, and
- Geohazard assessment in an active rift.

These objectives were and will be accomplished as a result of successful drilling, coring, and logging at three sites in the Gulf of Corinth, which collectively yielded 1645 m of recovered core over a 1905 m cored interval. Together, these cores provide (1) a long rift history (Sites M0078 and M0080), (2) a high-resolution record of the most recent phase of rifting (Site M0079), and (3) the spatial variation of rift evolution (comparison of sites in the central and eastern rift). The sediments contain a rich and complex record of changing sedimentation, sediment and pore water geochemistry, and environmental conditions from micropaleontological assemblages. The preliminary chronology developed by shipboard analyses will be refined and improved during postexpedition research, providing a high-resolution chronostratigraphy down to the orbital timescale for a range of tectonic, sedimentological, and paleoenvironmental studies. This chronology will provide absolute timing of key rift events, rates of fault movement, rift extension and subsidence, and the spatial variations of these parameters. The core data will also allow us to investigate the relative roles of and feedbacks between tectonics, climate, and eustasy in sediment flux, basin evolution, and basin environment. Finally, the Corinth rift boreholes will provide the first long Quaternary record of Mediterranean-type climate in the region. The potential range of scientific applications for this unique data set is very large, encompassing tectonics, sedimentary processes, paleoenvironment, paleoclimate, paleoecology, geochemistry, and geohazards.

¹ McNeill, L.C., Shillington, D.J., Carter, G.D.O., Everest, J.D., Le Ber, E., Collier, R.E.Ll., Cvetkoska, A., De Gelder, G., Diz, P., Doan, M.-L., Ford, M., Gawthorpe, R.L., Geraga, M., Gillespie, J., Hemelsdaël, R., Herrero-Bervera, E., Ismaiel, M., Janikian, L., Kouli, K., Li, S., Machlus, M.L., Maffione, M., Mahoney, C., Michas, G., Miller, C., Nixon, C.W., Oflaz, S.A., Omale, A.P., Panagiotopoulos, K., Pechlivanidou, S., Phillips, M.P., Sauer, S., Seguin, J., Sergiou, S., Zakharova, N.V., 2019. Expedition 381 summary. In McNeill, L.C., Shillington, D.J., Carter, G.D.O., and the Expedition 381 Participants, *Corinth Active Rift Development*. Proceedings of the International Ocean Discovery Program, 381: College Station, TX (International Ocean Discovery Program). <https://doi.org/10.14379/iodp.proc.381.101.2019>

² Expedition 381 Participants' affiliations.

MS 381-101: Published 28 February 2019

This work is distributed under the [Creative Commons Attribution 4.0 International](#) (CC BY 4.0) license. 

Introduction

How rifting initiates and evolves to continental breakup and ocean basin formation is a major unanswered solid earth/plate tectonics question; continental rifting is the first stage of this process. Numerical models indicate that strain rate is a key parameter controlling the style and magnitude of extension, but spatial and temporal patterns in strain rate are very poorly known for most extensional systems because of scarce chronological constraints, other than over short (earthquake-cycle) timescales. Key questions include the following: What controls rift geometry and evolution? How does activity on faults change with time? What does rift evolution and fault activity tell us about crustal rheology? What are the implications of changing fault activity for earthquake activity in a developing rift fault system? Over the last ~15 years, important insights have been derived from numerical models (e.g., Burov and Poliakov, 2001; Lavier and Buck, 2002; Lavier and Manatschal, 2006; Huismans and Beaumont, 2007, 2011; Olive et al., 2014) and from observations at mature, magma-poor passive margins where activity has ceased (e.g., Manatschal et al., 2001; Whitmarsh et al., 2001; Osmundsen and Ebbing, 2008; Van Avendonk et al., 2009; Bayrakci et al., 2016). However, early synrift stratigraphy is often difficult to image and sample because of deep burial and tectonic overprinting, making it difficult to examine the earliest stages of rifting.

Instead, this project studies the young, seismically active Corinth rift with a unique existing data set to resolve at high temporal and spatial resolution how rift faults initiate and link and how strain is distributed over time. The rift is currently a closed, small-scale sedimentary system, and the last ~1–2 My of the synrift stratigraphic record is preserved offshore, with earlier rift sediments preserved onshore, providing a clear spatial and temporal record of fault and rift activity. The Corinth rift is also an ideal target for studying rift processes because it is opening broadly orthogonally (perpendicular to the rift axis) at high strain rates (e.g., Briole et al., 2000), extension is localized, it lacks volcanism, and almost no tectonic overprinting occurs. Thus, the number of variables contributing to rift development are reduced, and a study here will complement research in other active rift systems that are more mature, oblique, and/or characterized by significant magmatism (e.g., East Africa and the Gulf of California).

Constraining the contributions of tectonics and climate to landscape evolution and sediment delivery in active basins and how surficial processes influence tectonics remains a major challenge in Earth science. Uplift and subsidence associated with rift faults can strongly modify landscapes, creating and destroying sediment delivery pathways into rift basins (e.g., Gawthorpe and Leeder, 2000), but a detailed record of a complete sedimentary system in a young, active rift is lacking. For example, how do strain rate and strain distribution control landscape development and sediment flux into rifts? Climate is clearly another dominant control on sediment flux. Isolated and semi-isolated active basins are particularly sensitive to climate and sea level change (e.g., Collier et al., 2000; Scholz et al., 2007; McHugh et al., 2008; Lyons et al., 2015); thus, active rift basins are ideal targets both for assessing how changing climate impacts sedimentation and for examining changes in paleoenvironment as basins repeatedly become isolated and reconnected to the global oceans as a result of glacial–interglacial cycles. Where strain rates are high, such as at the Corinth rift, high basin sediment accumulation rates provide a very high resolution record of regional climate, basin paleoenvironment, and change in sediment source and flux into the basin through time. Recent models predict that surface pro-

cesses will also influence rift development by modifying the thermal structure (Bialas and Buck, 2009) and by redistributing mass through erosion and deposition (Olive et al., 2014), all of which can influence fault evolution and strain localization. Resolving the interplay between these processes requires a detailed record of climate, tectonics, and sedimentation in a young rift basin. The Corinth rift is an excellent location to tackle these questions. In this region, glacial–interglacial cycles are characterized by changes in climate, sea level, and vegetation (e.g., Tzedakis et al., 2009; Sadori et al., 2016), allowing us to examine the impact of both climatic change and tectonics on surface processes. Sedimentation rates are high, and the geology around the Corinth rift is well studied, enabling a comprehensive study of the complete synrift sedimentary system.

During International Ocean Discovery Program (IODP) Expedition 381, a significant part of the synrift sequence of the Corinth rift was drilled, sampled, and logged to constrain in space and time (1) the deformation rate, (2) the absolute timing of rifting processes, (3) subsidence and sediment flux, (4) changing paleoenvironment and depositional conditions, and (5) the interaction of rift development and climate on surface processes and sediment flux.

Background Corinth rift

The Aegean Sea represents a natural laboratory for the study of rapid continental extensional tectonics. Extension began here in the Oligocene–Miocene (e.g., McKenzie, 1978; Le Pichon and Angelier, 1981; Jolivet et al., 1994; Armijo et al., 1996; Jolivet, 2001). In the late Pliocene–early Pleistocene, deformation became strongly localized across a few zones, and the Corinth rift was the most prominent zone (Figure F1). Debate continues on the origin of extension in the broader Aegean and focusing of strain at the Corinth rift, with models typically combining gravitational collapse of thickened crust, subduction-driven rollback, westward extrusion of Anatolia, and propagation of the North Anatolian fault (e.g., Armijo et al., 1996; Jolivet et al., 2010). Regional lithospheric structure, including crustal thickness and structure of the underlying subducting African plate, is constrained by wide-angle seismic and teleseismic tomographic techniques and gravity data (e.g., Tiberi et al., 2000; Sachpazi et al., 2007; Zelt et al., 2005); thicker crust (~40–45 km) runs northwest–southeast along the orogenic Hellenide/Pindos mountain belt in the western Corinth rift.

The active Corinth rift is a ~100 km × 30–40 km domain experiencing north–south extension, and the entire rift system is ~70–80 km wide. Geodetically measured extension rates over the last 25 yr reach 10–15 mm/yr (e.g., Clarke et al., 1998; Briole et al., 2000; Bernard et al., 2006), some of the highest in the world, giving strain rates of ~5 × 10⁻⁷/yr. The Corinth rift is also one of Europe's most seismically active areas.

Rift evolution and stratigraphy

Corinth rifting began at ~5 Ma with three main phases (1–3) identified by integration of onshore depositional records and offshore seismic stratigraphy (Figure F2) (e.g., Higgs, 1988; Armijo et al., 1996; Sachpazi et al., 2003; Ford et al., 2007, 2016; Bell et al., 2009; Taylor et al., 2011; Nixon et al., 2016; Gawthorpe et al., 2017). During Phase 1 (Pliocene), the initial basinal deposition (from onshore preserved sediments) was continental, varying from alluvial fans in the west to lacustrine in the east (Ford et al., 2007, 2013; Rohais et al., 2007; Hemelsdaël et al., 2017; Gawthorpe et al., 2017). The transition from Phase 1 to Phase 2 is marked by increased sub-

Figure F1. Corinth rift with primary rift-related faults (both active and currently inactive), multibeam bathymetry of the gulf, and Expedition 381 drill sites. Offshore fault traces are derived from Nixon et al. (2016), building on Bell et al. (2009) and Taylor et al. (2011). Onshore fault traces are derived from Ford et al. (2007, 2013) and Skourtsos and Kranis (2009). Bathymetry data provided by the Hellenic Centre for Marine Research and collected for R/V *Aegaeo* cruises (Sakellariou et al., 2007). Inset: tectonic setting of Corinth rift in Aegean region, Eastern Mediterranean Sea.

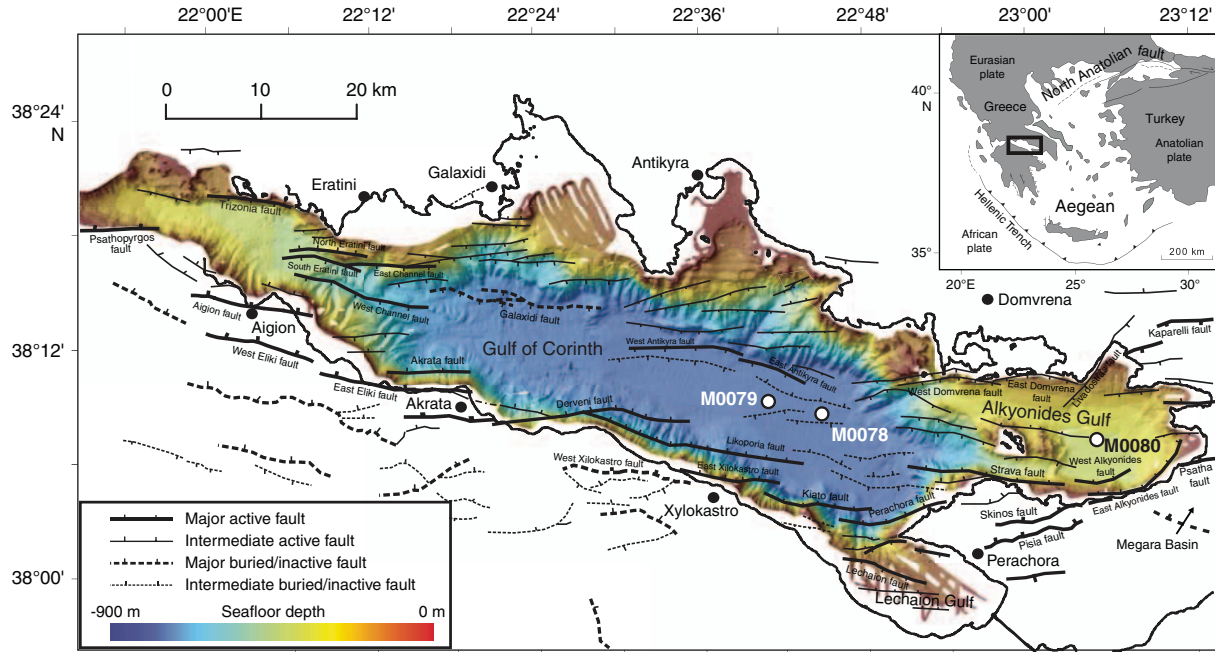
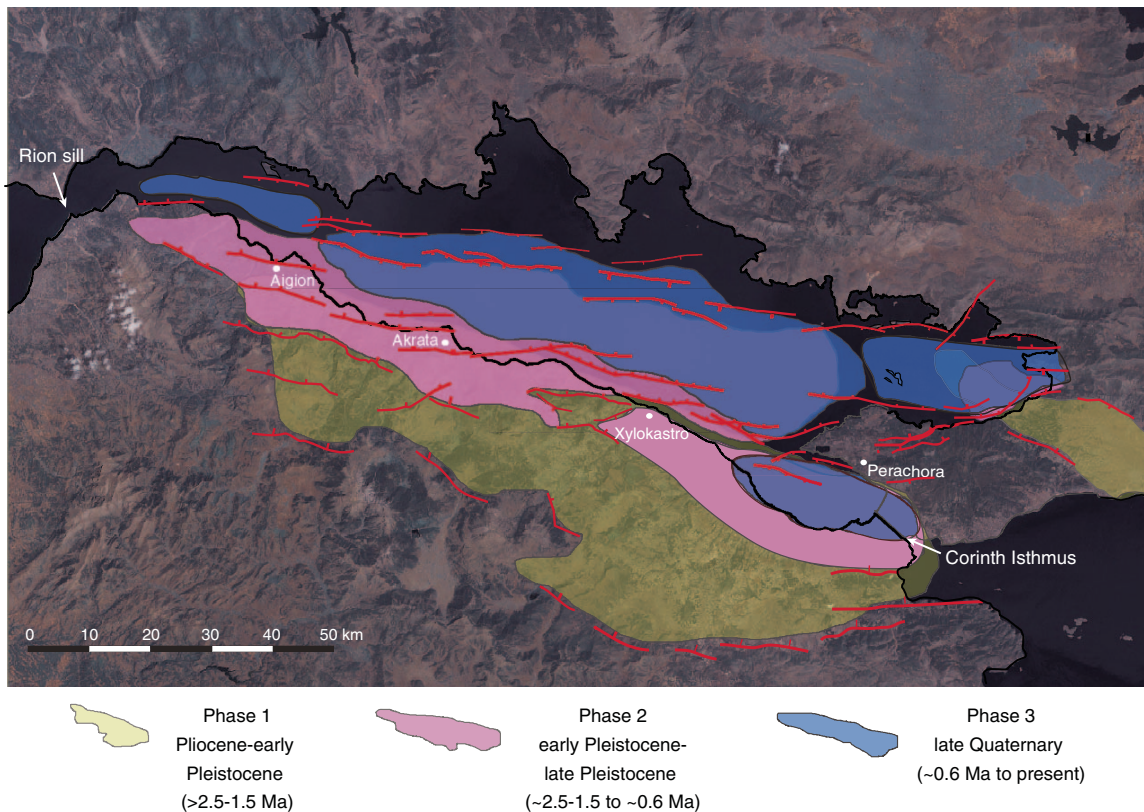


Figure F2. Summary of currently resolved distribution of deposits assigned to each of the three evolutionary rift phases of the Corinth rift system (Sakellariou and Lykousis, 2007) with simplified major faults overlain (see Figure F1 for map details). Sills bounding the Corinth basin that have controlled connection to the global oceans are also indicated (Isthmus of Corinth, Rion sill). Contributions from Ford et al. (2013), Nixon et al., (2016), Gawthorpe et al. (2017). Note that ages given are estimated from predrilling results.

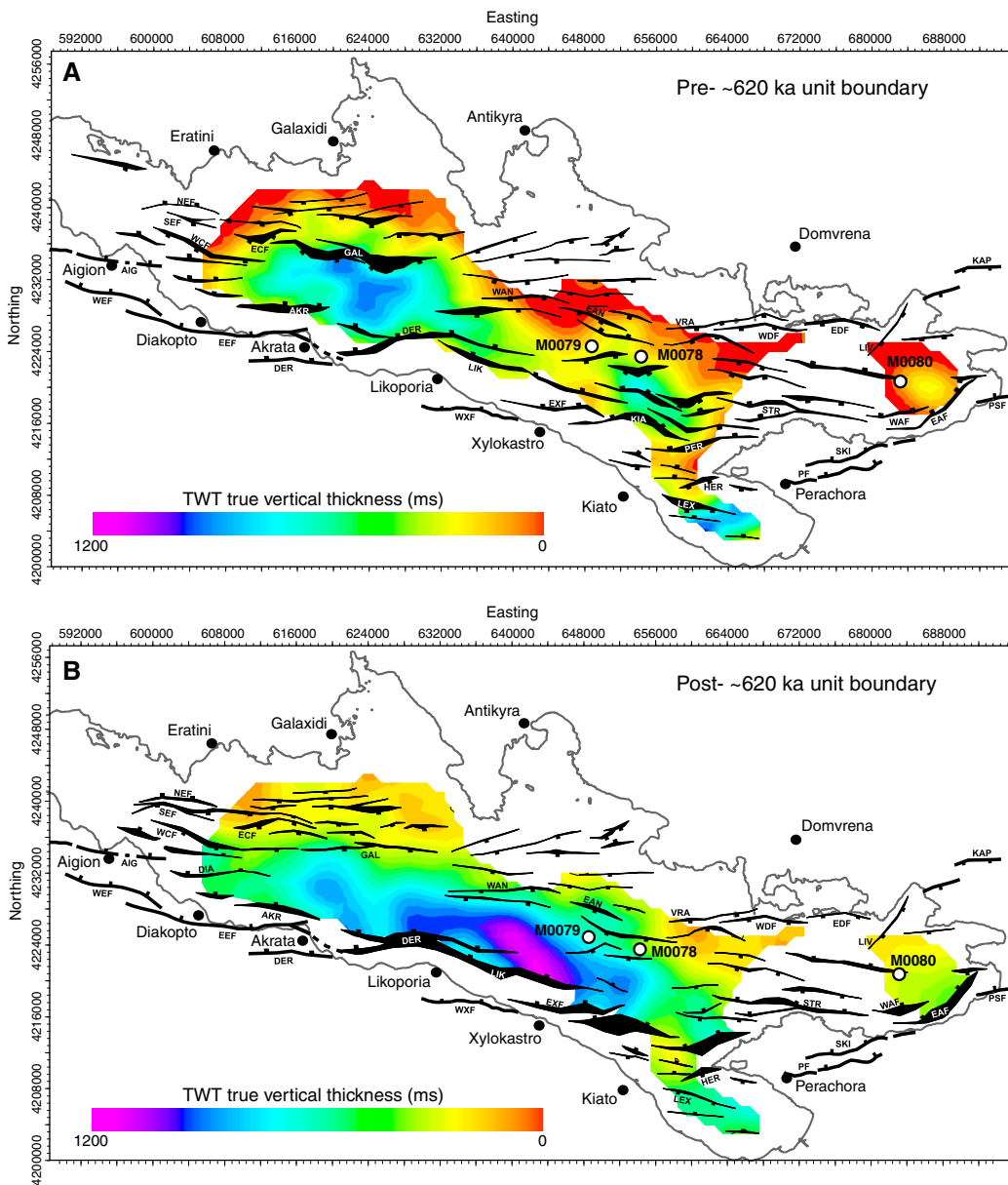


sidence rates and sediment supply, depocenter deepening and northward migration, and fault linkage and/or migration, with deposition of large marginal fan deltas (locally as thick as 800 m) during Phase 2 (“Middle Group” onshore; lower synrift unit [seismic Unit 1] offshore). These deltas are now uplifted and exposed onshore (Backert et al., 2010). The Phase 1–2 transition appears to have occurred at different times along the rift (e.g., ~2.2 Ma in the Alkyonides Gulf [eastern rift], ~3.0 Ma in the central rift [Leeder et al., 2008, 2012], and ~1.8 Ma in the western rift [Ford et al., 2013]).

During Phase 2, the rift was controlled by both south- and north-dipping faults (Bell et al., 2009; Ford et al., 2013, 2016; Nixon et al., 2016).

At ~0.6 Ma (hypothesized age prior to drilling), at the onset of Phase 3, fault activity again stepped northward and propagated westward, thus establishing the modern rift asymmetry with southern boundary north-dipping faults dominating subsidence (Figure F3). These southern boundary faults apparently grew and linked rapidly (Nixon et al., 2016). New fan deltas developed along the

Figure F3. Isochore maps for the two primary stratigraphic units of the offshore synrift succession with Expedition 381 sites. These two units are separated by a regional unit boundary or unconformity (compiled from Bell et al., 2009; Taylor et al., 2011; Nixon et al., 2016). A. Seismic Unit 1 (preregional unit boundary or unconformity, likely equivalent to onshore Middle Group, with an estimated age older than ~0.62 Ma). B. Seismic Unit 2 (postregional unit boundary or unconformity, likely equivalent to onshore Upper Group, with an estimated age younger than ~0.62 Ma). Represented faults are mainly those active during the time period shown. Age estimates are predrilling and based on seismic stratigraphic interpretations only. NEF = North Eratini fault, SEF = South Eratini fault, WCF = West Channel fault, ECF = East Channel fault, AIG = Aigion fault, GAL = Galaxidi fault, WEF = West Eliki fault, EEF = East Eliki fault, AKR = Akrata fault, DER = Derveni fault, WAN = West Antikyra fault, LIK = Likoporia fault, WXF = West Xylokaastro fault, EXF = East Xylokaastro fault, EAN = East Antikyra fault, KIA = Kiato fault, VRA = Vroma fault, PER = Perachora fault, LEX = Lechaion fault, HER = Heraion fault, WDF = West Domvrena fault, STR = Strava fault, PF = Pisias fault, EDF = East Domvrena fault, SKI = Skinos fault, LIV = Livadostras fault, WAF = West Alkyonides fault, EAF = East Alkyonides fault, KAP = Kaparelli fault, PSF = Psatha fault. TWT = two-way traveltime.



southern gulf margin (“Upper Group” onshore; upper synrift unit [seismic Unit 2] offshore). The rift environment during Phase 3 has long been hypothesized to alternate between isolated/semi-isolated (nonmarine) and marine between glacial and interglacial periods, respectively, as eustatic sea level fluctuated relative to the boundaries of the basin (e.g., Heezen et al., 1966; Sachpazi et al., 2003) (west: Rion sill; east: Isthmus of Corinth; Figure F2). The exact timing of onset of true marine deposition is not known but is hypothesized to correlate with the distinct seismic stratigraphy of the offshore upper synrift unit, seismic Unit 2 (Sachpazi et al., 2003; Bell et al., 2009; Nixon et al., 2016). However, earlier limited marine incursions have also been described (e.g., Bentham et al., 1991; Ford et al., 2007, 2013).

Overall, the Corinth rift appears to have migrated northward and possibly narrowed as it evolved (strain localization) (Figure F2). Geodetic and microseismicity data indicate that the highest modern strain rates are focused in the western rift (e.g., Avallone et al., 2004; Bernard et al., 2006), which is the youngest part of the rift (Ford et al., 2016). However, long-term extensional strain (on geological timescales) is greatest in the central rift (e.g., Bell et al., 2009, 2011). The extension rate may have increased at specific times over rift history (Ford et al., 2013, 2016), suggesting a deviation from models with relatively constant net strain and increasing, gradual localization (McLeod et al., 2000; Sharp et al., 2000; Gawthorpe et al., 2003; Taylor et al., 2004).

Offshore rift architecture and synrift stratigraphy

Patterns of extension in the offshore rift change along axis and with time, with changing polarity and symmetry of fault networks, single versus multiple active faults, and complex and changing depocenter geometry offshore (Figures F1, F3). Clear, traceable unit boundaries (possible unconformities or sequence boundaries) mark major changes in rift development in seismic reflection data, but their age is unknown.

The synrift succession offshore is locally as thick as ~2.5 km and divided into two seismic stratigraphic units (the older, lower amplitude seismic Unit 1 and the younger, well-stratified, and higher am-

plitude seismic Unit 2) separated by a unit boundary (U) that is locally angular and potentially unconformable (e.g., Figures F4, F5, F6, F7). Seismic Unit 1 includes two different seismic facies that may or may not be stratigraphically distinct: Subunit 1a (below), nonstratified (limited weak reflections) and mainly found on the southern basin margin, and Subunit 1b (above), more widespread and stratified (although weakly in places) (see Nixon et al., 2016). Seismic Unit 2 has been interpreted to record glacial–interglacial cycles on the basis of marine and lacustrine conditions detected in short cores (Moretti et al., 2004; Collier et al., 2000), clinof orm sequences on some basin margins (e.g., Leeder et al., 2005; McNeill et al., 2005; Lykousis et al., 2007; Bell et al., 2008), and alternating low-amplitude/high-amplitude seismic sequences interpreted to be low-stand lacustrine/highstand marine sequences, respectively (e.g., Sachpazi et al., 2003; Lykousis et al., 2007; Bell et al., 2008, 2009; Taylor et al., 2011) (e.g., Figure F5). The integrated sequence stratigraphic interpretations of the seismic reflection data network suggest the base of seismic Unit 2 is ~0.6 Ma (Nixon et al., 2016). The onshore Middle Group is thought to be time-equivalent to seismic Unit 1 offshore, with the onshore Upper Group equivalent to seismic Unit 2 offshore. The onshore “Lower Group” is likely of minimal thickness offshore, if present at all, because the primary locus of rifting at that time lay south of the present-day gulf (e.g., Figure F2). However, other Phase 1 rift depocenters (such as the Megara Basin; Figure F1; e.g., Bentham et al., 1991) may have extended northwestward into the present-day Alkyonides Gulf at the eastern end of the rift (Figure F1).

Depth to basement maps (Bell et al., 2009; Taylor et al., 2011) show a single depocenter below the current central gulf, with reduced subsidence in the eastern (Alkyonides Gulf) and western rift. Isochore maps of the synrift sediments (Figure F3; Bell et al., 2009; Taylor et al., 2011; Nixon et al., 2016) indicate that before the ~0.6 Ma unit boundary/unconformity separating seismic Units 1 and 2, two primarily symmetric depocenters existed, but since ~0.6 Ma, these depocenters have linked into a single depocenter, coincident with transfer of strain from south- to north-dipping faults (increased asymmetry). Specifically, a change in rift polarity was fol-

Figure F4. Composite seismic line comprising parts of R/V *Maurice Ewing* Lines 18, 42, and 22 (Taylor et al., 2011), with interpretations of basement (black dotted line) and boundary between seismic Unit 1 (below) and seismic Unit 2 (above) (blue dotted line) from Nixon et al. (2016). Inset: seismic line and drill site locations. CDP = common depth point.

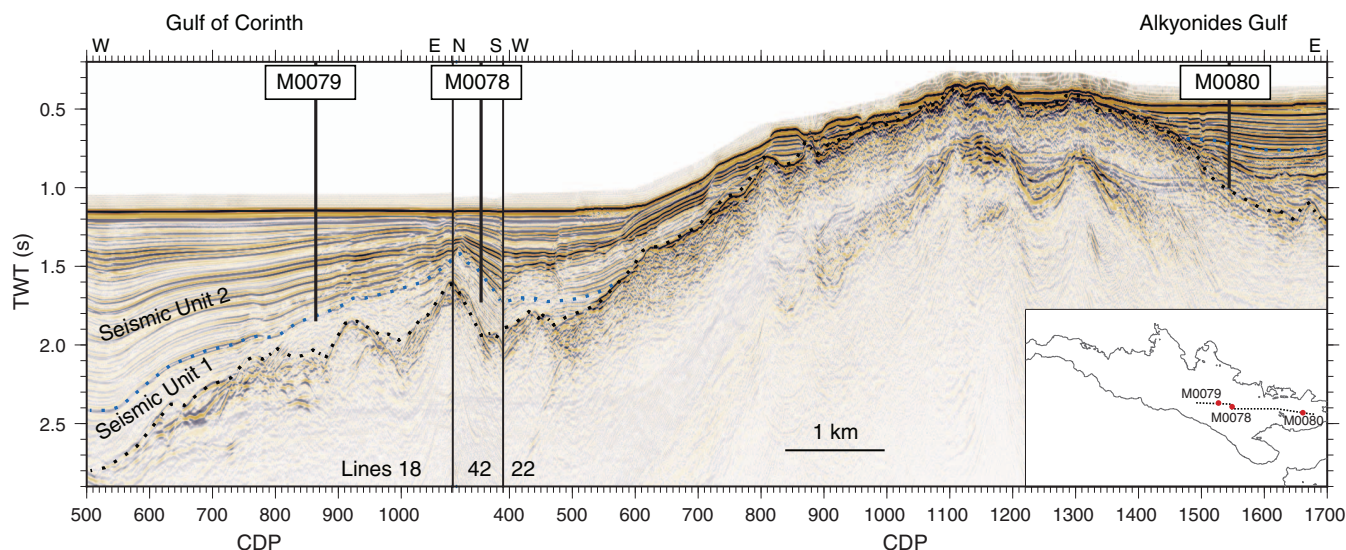


Figure F5. Site M0078 shown with *Maurice Ewing* Line 42 (Taylor et al., 2011) and interpretations from Nixon et al. (2016) (colored dotted lines and text). Inset: seismic line and drill site locations.

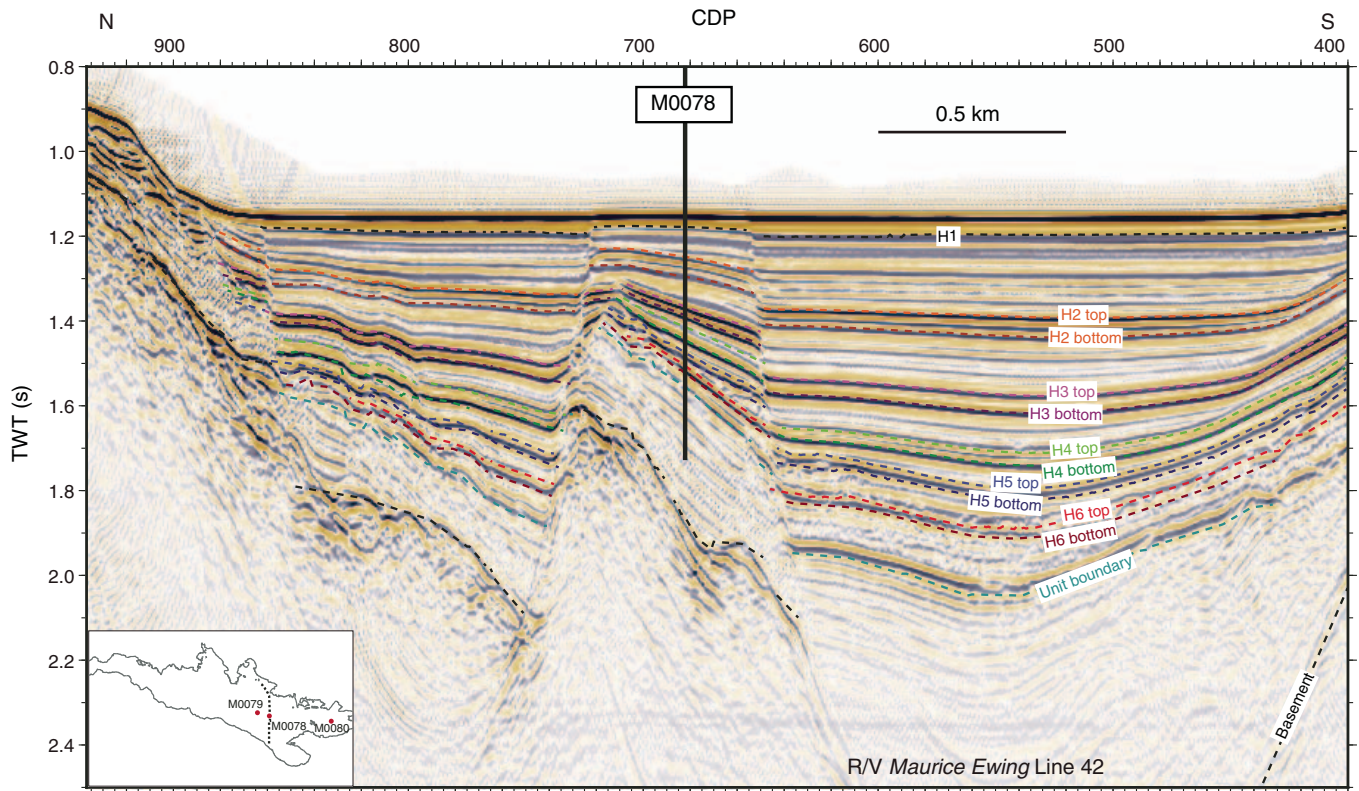


Figure F6. Site M0079 shown with *Maurice Ewing* Line 41 (Taylor et al., 2011) and interpretations from Nixon et al. (2016) (colored dotted lines and text). Inset: seismic line and drill site locations.

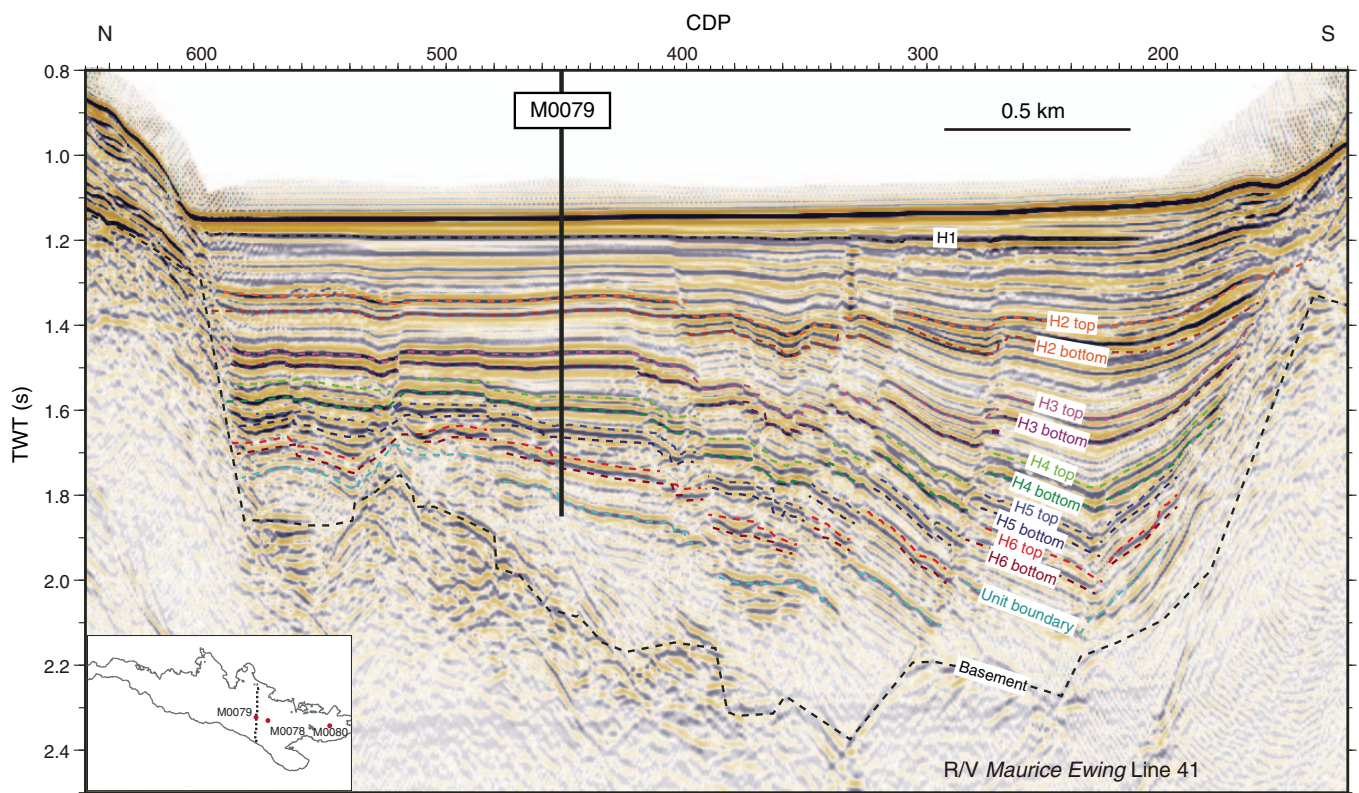
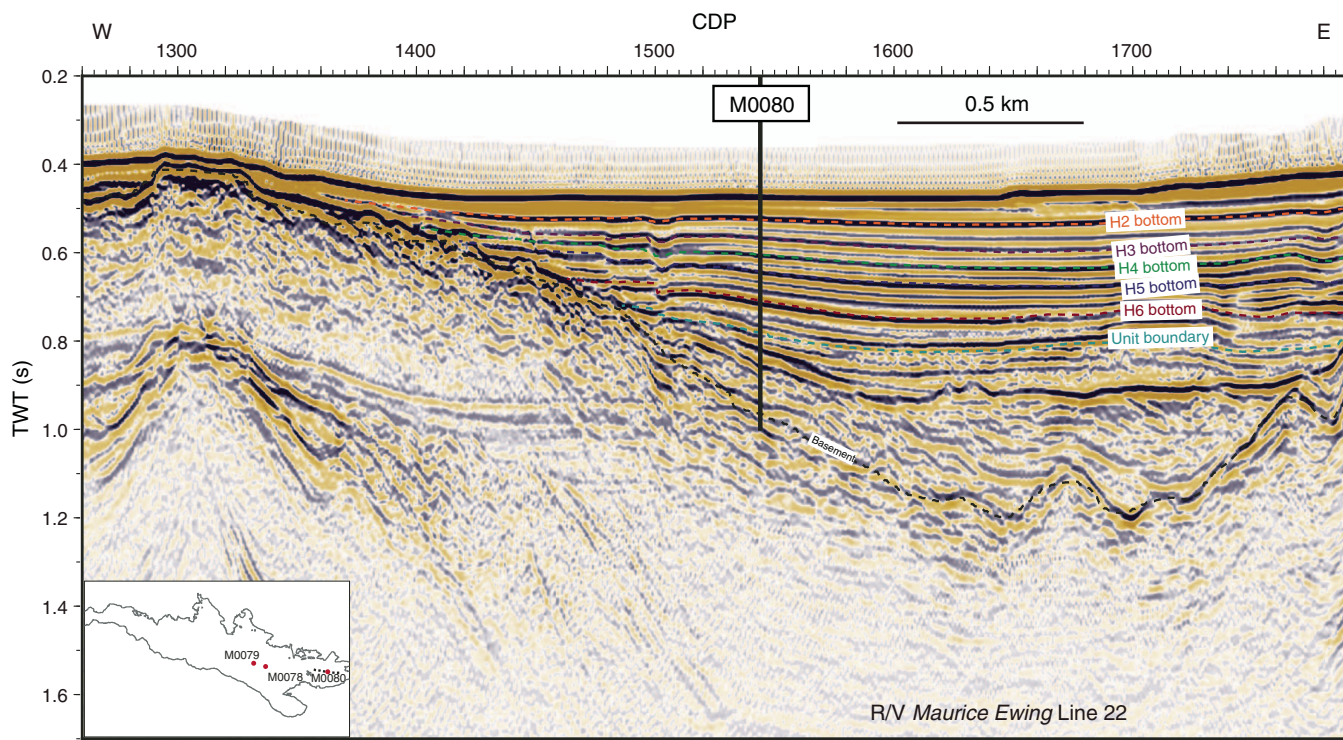


Figure F7. Site M0080 shown with *Maurice Ewing* Line 22 (Taylor et al., 2011) and interpretations from Nixon et al. (2016) (colored dotted lines and text). Inset: seismic line and drill site locations.



lowed by depocenter linkage. The switch to dominant north-dipping faults appears to be broadly synchronous along the entire rift. Since ~200 ka, these north-dipping faults appear to have evolved by linkage of smaller fault segments into longer fault segments and have increased in displacement and activity with equivalent changes to the associated depocenters. The actual timing and rate of switch in rift polarity and of fault and depocenter linkage can only be constrained by combining constraints on chronostratigraphy from drilling with the existing dense seismic network.

Changing paleoenvironment in the Corinth area

Prior to Expedition 381, minimal information was available on the impact of climate variations and resulting sea level changes on sedimentation and paleoenvironment in the Corinth rift. Existing constraints came from onshore studies (e.g., Andrews et al., 2007), piston cores as long as 30 m (e.g., Moretti et al., 2004), and high-resolution geophysical imaging (e.g., Perissoratis et al., 2000; Bell et al., 2009). Late Quaternary interglacial cycles in southeastern Europe are characterized by Mediterranean, sub-Mediterranean, and temperate forests, whereas glacial cycles are characterized by open woodland and steppes (e.g., Tzedakis et al., 2009; Sadori et al., 2016). Systematic fluctuations in marine microfossil assemblages and in the isotopic composition of their shells depict long- and short-term climatic changes in the region (Cita et al., 1977; Capotondi et al., 2016). In addition, these fluctuations provide valuable information regarding the impact of both African monsoon variability and higher latitude climate processes on the climatic and oceanographic evolution of the Eastern Mediterranean Sea (e.g., Rohling et al., 2015). Glacial–interglacial cycles appear to be associated with changes in sedimentary processes and environment in the Corinth basin (e.g., Perissoratis et al., 2000). For example, long piston cores that sample the most recent transition reveal changes in

sediment facies and micropaleontological assemblages (Moretti et al., 2004). The cores and data collected during Expedition 381 will provide unique constraints for examining the impact of both climatic change and tectonics on sedimentation and paleoenvironment in the gulf and improving understanding of regional climate in the Quaternary.

Objectives

Primary objectives

1. *Fault and rift structural evolution in an active continental rift: to establish the distribution of tectonic strain in time and space and the timescales of fault evolution in a young rift at high resolution (20–50 ky and one to tens of kilometers).*

We will determine the growth and development of a rift-scale normal fault network, timescales of rift segment establishment, basin evolution in terms of strain localization, rift propagation and migration, and the impact of crustal structure and composition on strain rate and distribution. What are the controlling parameters on strain localization? How and when does a “mature” fault network emerge? How does fault evolution impact subsidence patterns and depocenter development?

2. *Surface processes in active rifts: to determine the evolution of a rift-controlled, closed drainage system in time and space at high temporal resolution (20–50 ky) and the relative impact of tectonics and climate on sediment flux.*

What are the relative contributions of millennial to orbital periodicity Quaternary climate fluctuations (global and regional) and fault activity/rift evolution in controlling the supply of sediment into a rift basin? We will assess changes in sediment flux at a range

of timescales and analyze the paleoenvironment of the rift basin through time. These results will be used to evaluate the response of sediment supply to fault birth, death and migration, rift flank uplift, and changes in strain rate and to better understand feedbacks between climate, sea level fluctuation, erosion, sediment transport, and depositional and tectonic processes.

Secondary objectives

3. *To resolve reliable active fault slip rates to improve regional assessment of hazards due to earthquakes and secondary tsunami and landslides.*

The Gulf of Corinth has high levels of seismicity and damaging historic secondary hazards, such as slope failure and tsunami, in a region of high coastal population density. Fault slip rates currently rely on paleoseismological and tectonic geomorphological studies with dated materials of very recent fault slip (the last ~200 ky or less) and estimated horizon ages for longer timescales. These slip rate estimates include significant uncertainties, and slip rates remain unquantified on many faults. Ocean drilling allows us to determine fault slip rates on timescales of 10–100 ky to 1 My. We will integrate fault slip rates with shorter timescale data (paleoseismological, geodetic, and seismicity) to more fully understand the seismic hazard potential of individual faults. Cores may also allow us to assess the frequency of major slope failures (integrated with seismically identified mass transport deposits offshore), an indication of secondary hazards and of possible seismicity.

4. *To generate a new high-resolution record of the Quaternary paleoclimate of the Eastern Mediterranean Sea with respect to global climate and the paleoenvironment of the Corinth basin as a semi-isolated basin controlled by changing base level and climate.*

Details of the Corinth basin's changing environment from glacial to interglacial times are poorly known, and the precise timing and nature of transitions between isolated and marine conditions is unconfirmed, as is the relationship to the interacting controls of basin subsidence, sill elevation, and eustatic sea level. Offshore drilling of synrift sediments should provide a record of regional Quaternary paleoclimate and basin paleoenvironment by sampling and analyzing pollen, micro- and macrofossils, stable isotopes, and sediment physical and chemical properties. Long cores from the Gulf of Corinth should also provide the opportunity to generate (1) the first high-resolution relative paleointensity (RPI) record in the Mediterranean Sea correlated with global RPI stacks (e.g., Valet et al., 2005; Channell et al., 2009) and the pattern of the magnetic excursions (Stott et al., 2002; Lund et al., 2005; Channell et al., 2008) to help understand the dynamics of the geomagnetic field and (2) a linked terrestrial pollen and marine $\delta^{18}\text{O}$ record in the Eastern Mediterranean Sea (at least for interglacial intervals) to establish a record of paleoenvironment and vegetation and to help constrain age models for existing Eastern Mediterranean long pollen records.

Operational strategy

Based on seismic and bathymetric data acquired in the Gulf of Corinth prior to the expedition, three primary and three alternate drill sites were proposed to satisfy the objectives of the proposal. The three primary (and ultimately drilled) sites (Figure F1) were selected based on the likelihood of recovering key stratigraphic units to achieve the expedition scientific objectives, the ability to cor-

relate with horizons in the seismic reflection data network, and, in combination, to resolve both temporal and spatial rift evolutionary history.

Site M0078 (proposed Site COR-02A) is located in the central basin on a horst block where a relatively condensed section is expected. This site allows recovery of a long synrift record, including a significant part of seismic Unit 1 below, a near-complete seismic Unit 2 above, and the regional unit boundary or unconformity between them (Figures F4, F5). Site M0079 (proposed Site COR-01A) allows sampling of a complete seismic Unit 2 at very high resolution (Figures F4, F6). Site M0080 (proposed Site COR-04B) was selected because the uppermost basement and early seismic Unit 1 sediments can be sampled at this location because of the relatively thin seismic Unit 2 section (Figures F4, F7). The location of Site M0080 in the eastern part of the rift (Alkyonides Gulf; Figure F1) also provides an opportunity to test along-axis variation in rift processes.

All holes were sited in a 20 m radius of the proposed drilling sites approved by the IODP Environmental Protection and Safety Panel, with Holes M0078A, M0079A, and M0080A all situated within 5 m of the specified coordinates. The general locations of the sites drilled are shown in Figure F1. As with all mission-specific platform expeditions, no cores were split during the offshore phase; therefore, a comprehensive onshore phase complemented the offshore phase. Table T1 summarizes the descriptions and measurements made during Expedition 381 and indicates whether they were conducted offshore or onshore.

Offshore operations

Mobilization of the vessel began on 3 October 2017 in Falmouth, UK, with the D/V *Fugro Synergy* sailing for the Port of Valletta, Malta, on 7 October. On 16 October, the vessel arrived at the Port of Valletta, and European Consortium for Ocean Research Drilling (ECORD) Science Operator (ESO) personnel joined the vessel to continue the mobilization of science facilities before arrival in Greece. Following refueling, the *Fugro Synergy* continued the transit to the Port of Corinth, Greece, and was alongside on 19 October.

The offshore phase took place from 19 October to 18 December. The vessel sailed from Corinth on 22 October and returned to port on 18 December. Following completion of operations at Site M0078, a ~12 h port call was made in the Port of Corinth on 13 November for *Fugro/ESO* crew change and to load supplies and equipment. Demobilization also took place at the Port of Corinth, where the ESO refrigerated (reefer) containers, containerized laboratories, Multi-Sensor Core Logger (MSCL) laboratory container, and office containers were offloaded from the vessel in preparation for road transport to the Center for Marine Environmental Sciences (MARUM), University of Bremen (Germany), and transfer to Piraeus, Greece, for shipping by sea to the British Geological Survey (UK). The University of Montpellier logging container was transported by sea to Falmouth (UK) and then over land to Montpellier. ESO staff departed by 19 December following completion of demobilization.

The cores, core catcher samples, headspace gas samples, and interstitial water splits collected offshore were transported under refrigeration to the IODP Bremen Core Repository at MARUM (University of Bremen, Germany).

In total, 52.5 days of Expedition 381 were spent operational on station, 0.5 days were spent in transit between sites, 0.8 days were spent in port during the expedition, 0.2 days were spent on standby at station because of weather, and 2.3 days were spent on equip-

Table T1. Onshore and offshore measurements, Expedition 381. BCR = Bremen Core Repository. IW = interstitial water, ICP-OES = inductively coupled plasma-optical emission spectrometry, IC = ion chromatography, DIC = dissolved inorganic carbon, TOC = total organic carbon, TC = total carbon, LECO = carbon/sulfur analyzer, XRF = X-ray fluorescence, ED-XRF = energy dispersive XRF, MSCL = Multi-Sensor Core Logger, XRD = X-ray diffraction, CPT = cone penetration test, OSP = Onshore Science Party. [Download table in CSV format.](#)

D/V <i>Fugro Synergy</i> , offshore Corinth	Onshore Science Party, BCR (Germany)
Core description: through-liner observation and description of core catchers and split whole rounds	Core description: split-core visual core description (sedimentological and structural) and smear slide analysis
Micropaleontology: diatoms, nannofossils, and foraminifers	Micropaleontology: foraminifers, palynology, diatoms, and nannofossils
Geochemistry IW analysis: pH by ion-specific electrode, alkalinity by single-point titration to pH, salinity by refractometer, ammonium by flow injection method, and sampling for postexpedition research for time-sensitive analyses	Geochemistry IW analysis: ICP-OES (major and trace elements), IC (anions), phosphate, and DIC
Whole-core MSCL logging: density, <i>P</i> -wave velocity, magnetic susceptibility, electrical resistivity, and natural gamma radiation	Geochemistry solid phase analysis: TOC/TC by LECO (carbon-sulfur analysis) and XRF bulk element analysis by ED-XRF
Core catcher photography	XRD bulk mineralogy analysis
Downhole logging: total natural gamma, spectral gamma, resistivity, sonic, conductivity, and magnetic susceptibility	Discrete sample measurements: moisture and density properties (bulk and grain density and water content porosity), and compressional <i>P</i> -wave velocity
Shear strength (handheld penetrometer and downhole CPT)	Core imaging
Downhole temperature (CPT)	Shear strength (shear vane and fall cone)
	High-resolution continuous digital line scanning of all split-core surfaces
	Thermal conductivity on whole cores (pre-OSP)
	Split-core MSCL logging: color reflectance and <i>P</i> -wave measurements
	Discrete paleomagnetic measurements and discrete magnetic susceptibility measurements
	Core XRF scanning (post-OSP)

Table T2. Hole locations, water depths, core, and operational information, Expedition 381. [Download table in CSV format.](#)

Hole	Latitude	Longitude	Water depth (mbsl)	Core runs	Interval cored (m)	Interval recovered (m)	Core recovery (%)	Interval open holed (m)	Penetration depth (mbsf)	Time on site (days)
M0078A	38°8'41.802"N	22°45'30.251"E	859.5	176	610.43	533.99	87	0	610.43	20
M0078B	38°8'41.144"N	22°45'30.242"E	864.0	15	55.85	52.17	93	0	55.85	1
M0079A	38°9'30.243"N	22°41'43.316"E	857.1	163	704.90	610.80	87	0	704.90	18
M0080A	38°7'12.147"N	23°5'10.614"E	348.8	146	534.10	447.83	84	0	534.10	16

ment-related downtime. See Table T2 for a summary of offshore operations and core recovery. Shipboard-generated core recovery plots are available in the weekly ship reports on the ECORD Expedition 381 website (<http://www.ecord.org/expedition381/reports>).

The following coring and downhole logging tools were available during Expedition 381:

- Fugro Wison Extended Piston (WEP) system (designated core type "H"),
- Fugro Corer system in push mode (designated core type "P") and percussive mode (designated core type "V"),
- Fugro Extended Marine Core Barrel (FXMCB) system (rotary; designated core type "R"),
- DOSECC Exploration Services suite of coring tools as a backup, and
- A suite of standalone and stackable slimline wireline logging tools (from the University of Montpellier and operated by the European Petrophysics Consortium).

Onshore Science Party

Thermal conductivity measurements were carried out every ~10 m on the cores from all sites before the start of the Onshore Science Party (OSP).

During the Expedition 381 OSP from 31 January to 28 February 2018, the cores were described in detail and IODP standard sampling and measurements and postexpedition scientific research sampling were undertaken (Table T1). Analytical laboratories and equipment were used at MARUM (nondestructive core logging, marine geotechnics, inorganic geochemistry, and microscopes) and the Department of Geosciences at the University of Bremen (paleo-

magnetism and hydrofluoric acid laboratories and the carbon/sulfur analysis system).

Principal results

Operational site summaries

Site M0078

Site M0078 is located in the central Gulf of Corinth (Figure F1) on a fault-bounded horst block (Figure F5) with the aim of recovering a long, condensed record of synrift sedimentation. Two holes (M0078A and M0078B) were drilled at water depths of 859.5 and 864.0 meters below sea level (mbsl), respectively. Hole M0078A was drilled and cored to 610.43 meters below seafloor (mbsf) using the Fugro WEP system (piston), the Fugro Corer in push and percussive modes, and the FXMCB (rotary corer). Core recovery was 87%. Downhole logging was attempted in Hole M0078A, but successful data collection was not possible. Hole M0078B was drilled and cored to 55.85 mbsf using the Fugro Corer in push mode to capture material not recovered in Hole M0078A. Core recovery was 93%. Downhole logging was not conducted in Hole M0078B because it was a relatively shallow hole.

Site M0079

Site M0079 is located in the central Gulf of Corinth (Figure F1) with the aim of drilling a complete and expanded stratigraphic section of the most recent rift phase and the uppermost section of sediments from the penultimate phase to provide a high-resolution temporal record (Figure F6). Hole M0079A (water depth of 857.1 mbsl) was drilled and cored to 704.9 mbsf using the Fugro Corer in push and percussive modes and the FXMCB. Core recovery was

87%. Downhole logging was conducted with a limited suite of logging tools, primarily in the upper 295 mbsf.

Site M0080

Site M0080 is located in the Alkyonides Gulf (Figures F1, F7) in the eastern part of the Corinth rift with the aim of testing spatial variation in rift evolution history and to sample earlier phases of rifting. Hole M0080A (water depth of 348.8 mbsl) was drilled and cored to 534.1 mbsf using the Fugro Corer in push and percussive modes and the FXMCB. Core recovery was 84%. Downhole logging was conducted with a full suite of standard logging tools, with most depth intervals covered.

Lithostratigraphy

The drilled sequences of Expedition 381 comprise an upper section (lithostratigraphic Unit 1 at Sites M0078 and M0079; lithostratigraphic Units 1 and 2 at Site M0080) that records the most recent phase of synrift deformation and deposition (equivalent to seismic Unit 2), a lithostratigraphic unit boundary (of possible unconformable nature in places), and an underlying unit or units (lithostratigraphic Unit 2 at Sites M0078 and M0079; lithostratigraphic Units 3 and 4 at Site M0080; equivalent to seismic Unit 1) that record(s) earlier rift history and represents a variable time period of deposition. The lithostratigraphic units for all sites were defined based on lithologic, micropaleontological, and select physical properties. To characterize the lithostratigraphy, a series of facies associations (FAs) were defined based on physical and biogenic features of the sediment, including bedding and lamination style, grain size, color, and body and trace fossils. The facies associations are defined in Table T3 and described in the [Expedition 381 facies associations](#) chapter (McNeill et al., 2019).

Site M0078

The lithostratigraphy of Site M0078 is divided into two units with a boundary at 385.14 mbsf. Unit 1 (the upper unit) is divided into 16 subunits (Figure F8); micropaleontological data define these subunits as marine and isolated/semi-isolated intervals that appear to be primarily controlled by changing eustatic sea level with respect to sills at the entrance to the Corinth basin.

Unit 1 sediments are dominated by detrital clay- and silt-grade carbonate. Background sedimentation consists of hemipelagic and turbiditic muds with occasional thin, coarser (fine silt to medium sand) beds and turbidite–homogeneous mud couplets. Bioturbation is primarily present in the marine subunits. Calcite is the most abundant mineral, with common to abundant quartz, feldspars, and micas. Biogenic material is common (in particular in the marine subunits), as are organic components and framboidal pyrite. Well-sorted, silt-sized aragonite needles are dominant in some laminated intervals. Marine subunits in Unit 1 (odd numbers) are dominated by homogeneous to poorly bedded, often greenish gray mud (FA1 and FA6; see Table T3) with some laminated muds (e.g., FA3) and sparse thin silty and sandy beds. Isolated/semi-isolated subunits (even numbers) include laminated muds, thin mud beds, greenish gray mud with homogeneous thick mud beds, and dark gray to black organic-rich beds (FA4, FA3, and FA5) with sparse thin silty and sandy beds. Submillimeter- to millimeter-scale laminations, commonly gray to white, also occur in these isolated/semi-isolated subunits (FA3). Throughout Unit 1, interbedded mud–silt and centimeter-thick sand beds are present, but overall sand is a minor component and decreases with depth (Figure F8).

Unit 2 has a composition similar to that of Unit 1, with calcite the dominant mineral. This unit is composed almost entirely of light

Table T3. Definitions of facies associations used in lithostratigraphic interpretation, Expedition 381. [Download table in CSV format.](#)

Facies association	Definition
FA1	Homogeneous mud
FA2	Greenish gray mud with dark gray to black mud to sand beds and laminations
FA3	Light gray to white laminations alternating with mud and silt beds
FA4	Laminated greenish gray to gray mud with mud beds
FA5	Greenish gray mud with homogeneous centimeter-thick gray mud beds
FA6	Green bedded partly bioturbated mud, silt, and sand
FA7	Clast-supported sandy conglomerates and pebbly reddish brown sand with silt
FA8	Reddish brown to brownish gray mud and/or silt, including mottled textures and rootlets
FA9	Green-gray, often pebbly sandstone/siltstone
FA10	Interbedded mud/silt and decimeter-thick sand beds
FA11	Interbedded mud/silt and centimeter-thick sand beds
FA12	Light gray to buff homogeneous to weakly stratified bioturbated mud
FA13	Contorted bedding and mud-supported sand and conglomerates
FA14	Greenish gray pebbly silt and clast-supported fining-upward conglomerates
FA15	Greenish to buff bioclastic laminated siltstone to bedded fine sandstone, including bioturbation, ostracods, and rootlets
FA16	Greenish to buff bedded and bioturbated bioclastic sandstone to mudstone
FA17	Greenish laminated to faintly bedded/homogeneous fossiliferous mudstone

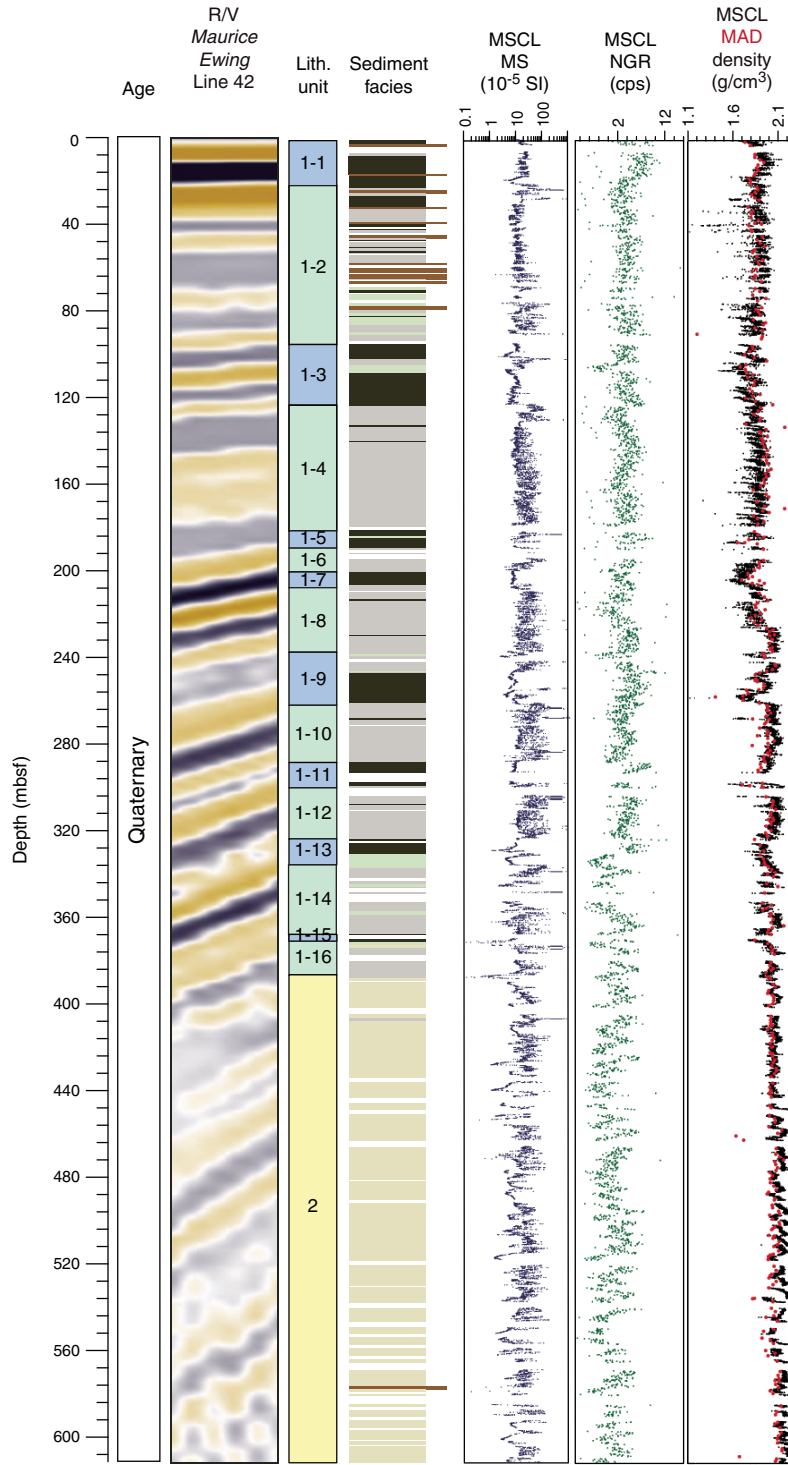
gray or buff weakly laminated to homogeneous highly bioturbated mud (FA12; Figure F8). Minor darker gray mud with faint bedding and black laminations also occurs. The Unit 1/2 boundary is sharp and marked by an abrupt change from laminated greenish gray muds to homogeneous light gray muds downhole.

Site M0079

The lithostratigraphy of Site M0079 is divided into two units with a boundary at 677.23 mbsf (Figure F9). Unit 1 is divided into 16 subunits that micropaleontological data define as alternating marine and isolated/semi-isolated intervals. As at Site M0078, Unit 1 sediments are dominantly fine grained and carbonate rich. Detrital calcite predominates, with subordinate quartz, feldspar, and phyllosilicates. Biogenic material is common, particularly in the marine subunits. Depositional processes were dominated by fine-grained turbiditic and hemipelagic deposition. Marine subunits in Unit 1 (odd numbers) are moderately to highly bioturbated and dominated by homogeneous to poorly bedded greenish gray muds (FA1 and FA6; see Table T3). Isolated/semi-isolated subunits (even numbers) are dominated by laminated to thinly bedded gray and greenish gray muds, some with black, organic-rich laminations and beds (FA2, FA4, and FA5) with no or sparse bioturbation. Higher energy depositional processes are indicated by intervals of soft-sediment deformation and mud-supported conglomerates (FA13) and sand–homogeneous mud couplets that occur in both marine and isolated/semi-isolated units. Overall, occurrence of slumped and mud-supported conglomerates increases with depth in Unit 1, with a particularly thick slumped interval occurring in Subunit 1-11.

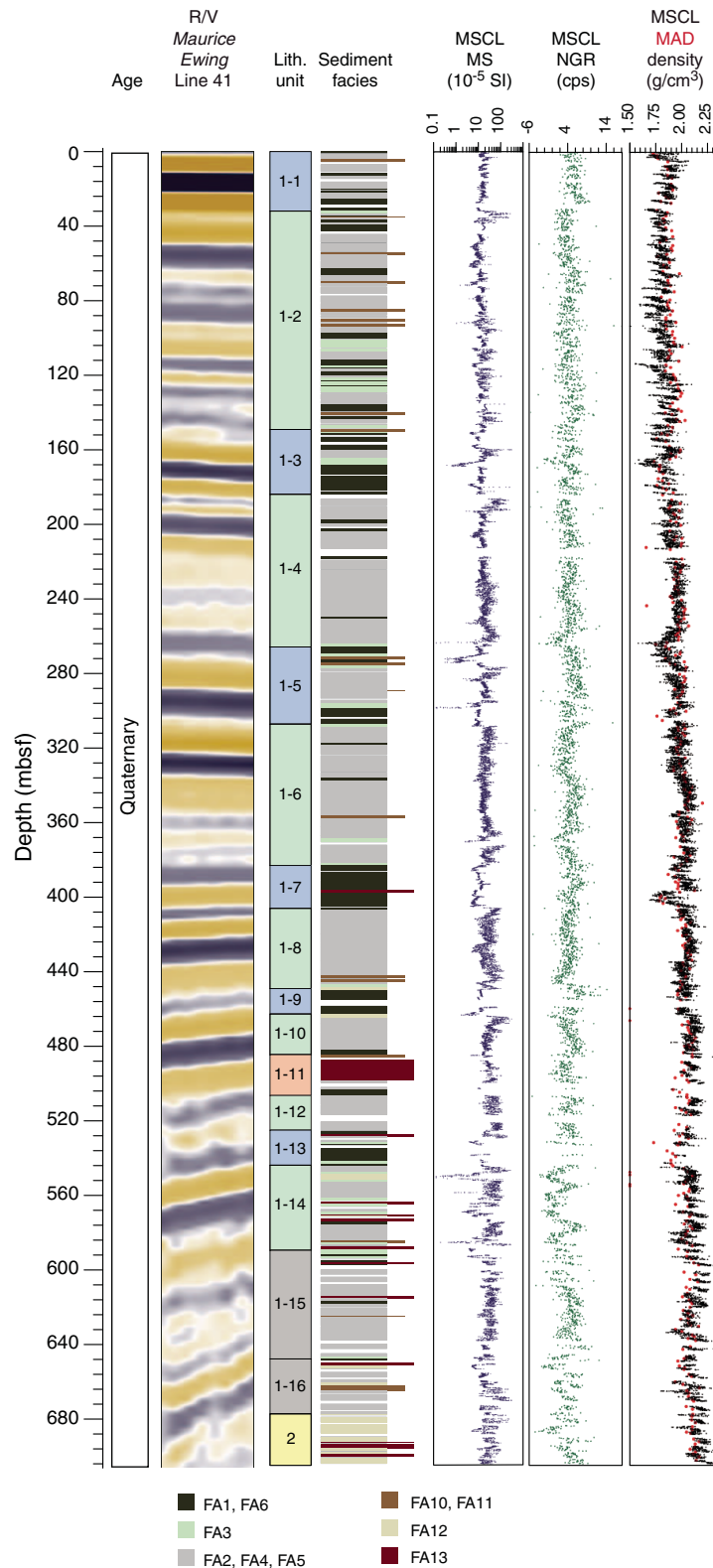
Unit 2 has a composition similar to that of Unit 1 and is dominated by light gray to buff weakly laminated to homogeneous highly bioturbated mud (FA12; Figure F9). It is also dominated by fine silt-sized detrital calcite, similar to Site M0078, with lower concentrations of siliciclastic grains compared with Unit 1. In contrast to Site M0078, Unit 2 contains fining-upward sands (FA10), many more sand and homogeneous mud couplets, and large decimeter- to meter-scale slump structures and mud-supported intraclast conglomerates (FA13).

Figure F8. Summary of geophysical data and lithostratigraphy, Site M0078. Seismic reflection data crossing site location from Taylor et al. (2011); borehole lies on right-hand side of image. Lithostratigraphic units and Unit 1 subunits with paleoenvironment: blue = marine, green = isolated/semi-isolated; Unit 2 shading is for visual differentiation and does not have any paleoenvironmental meaning. Assigned facies associations (FAs; see key) are from lithostratigraphic interpretations (some facies associations are grouped for simplicity and coarser sediment layers are highlighted by longer bars); see Table T3 for description of facies associations. MSCL magnetic susceptibility (MS), NGR, and density data are from whole cores. MAD bulk density data are from discrete core samples. cps = counts per second.



- FA1, FA6
- FA3
- FA2, FA4, FA5
- FA10, FA11
- FA12

Figure F9. Summary of geophysical data and lithostratigraphy, Site M0079. Seismic reflection data crossing site location from Taylor et al. (2011); borehole lies on right-hand side of image. Lithostratigraphic units and Unit 1 subunits with paleoenvironment: blue = marine, green = isolated/semi-isolated, gray = undetermined, pink = slumped interval; Unit 2 shading is for visual differentiation and does not have any paleoenvironmental meaning. Assigned facies associations (FAs; see key) are from lithostratigraphic interpretations (some facies associations are grouped for simplicity and coarser sediment layers are highlighted by longer bars); see Table T3 for description of facies associations. MSCL MS, NGR, and density data are from whole cores. MAD bulk density data are from discrete core samples.



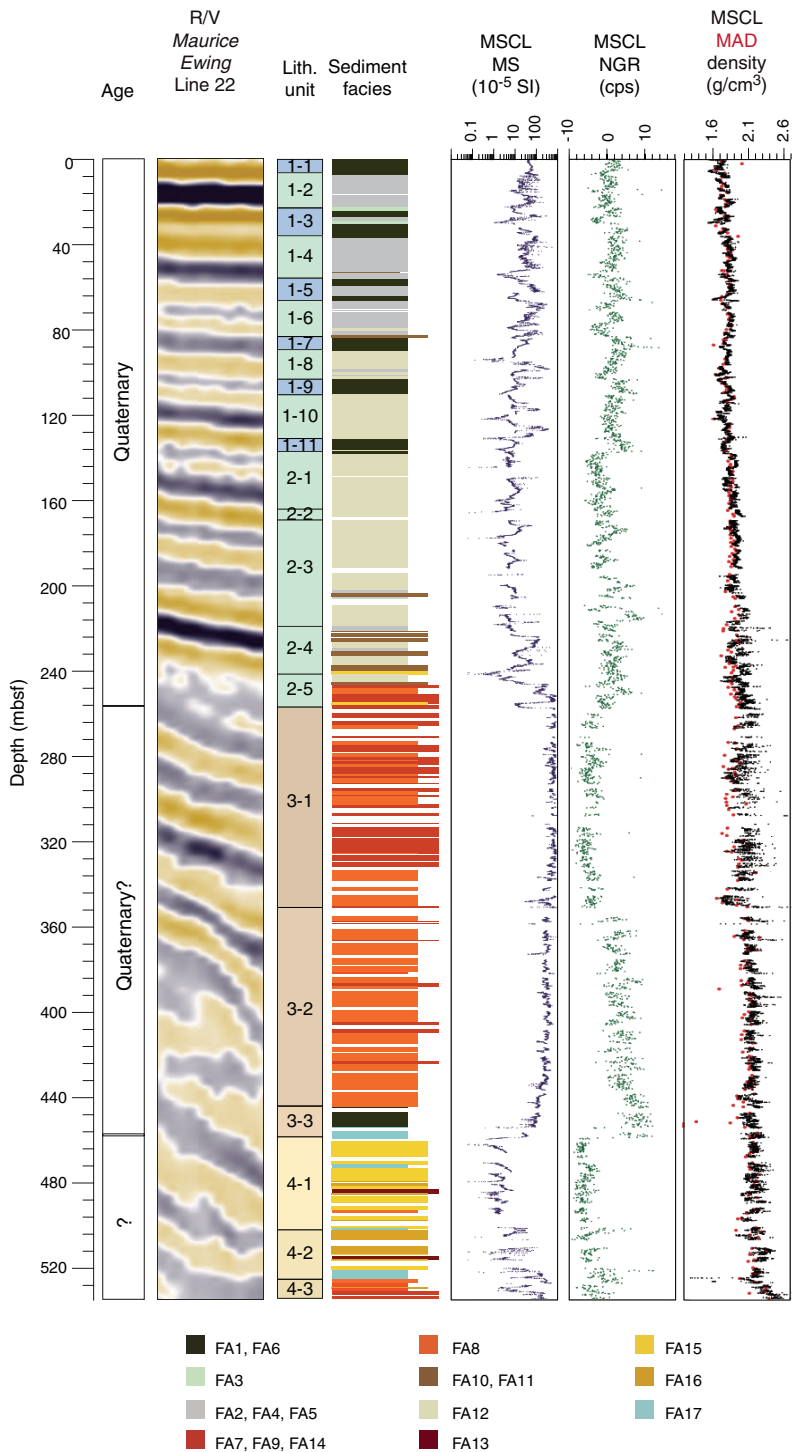
Site M0080

The lithostratigraphy of Site M0080 is divided into four units with boundaries at 136.96, 256.85, and 458.40 mbsf (Figure F10). Units 1 and 2 are dominated by moderately sorted, clay-grade calcite. Other minor terrigenous components include quartz, mica,

and feldspar mineral grains. Occasionally, both calcite and aragonite occur in equal proportions. Biogenic components and framboidal pyrite are common throughout.

Unit 1 has characteristics similar to those of Unit 1 at Sites M0078 and M0079 and is divided into 11 subunits based on alterna-

Figure F10. Summary of geophysical data and lithostratigraphy, Site M0080. Seismic reflection data crossing site location from Taylor et al. (2011); borehole lies on right-hand side of image. Lithostratigraphic units and Unit 1 subunits with paleoenvironment: blue = marine, green = isolated/semi-isolated; Unit 2, 3, and 4 shading is purely for visual differentiation and does not have any paleoenvironmental meaning. Assigned facies associations (FAs; see key) are from lithostratigraphic interpretations (some facies associations are grouped for simplicity and coarser sediment layers are highlighted by longer bars); see Table T3 for description of facies associations. MSCL MS, NGR, and density data are from whole cores. MAD bulk density data are from discrete core samples.



tions between dominantly bioturbated homogeneous and poorly bedded greenish gray and gray mud (FA1 and FA6) and bedded and laminated mud (FA2, FA3, FA4, and FA5) (Figure F10). These sediments are interpreted to be dominantly deep-water turbiditic and hemipelagic deposits. The alternating subunits are interpreted to represent alternating marine (homogeneous mud; FA1 and FA6) and isolated/semi-isolated (bedded and laminated mud; FA2, FA3, FA4, and FA5, and in lower even-numbered subunits light gray to buff weakly laminated to homogeneous highly bioturbated mud [FA12]) environments. Unit 2 is divided into an upper part dominated by light gray bioturbated mud (FA12) and a lower part with greater variability of facies and grain size, including ophiolitic-rich conglomerates, highly bioturbated mudstones with shallow-water foraminifer assemblages, and occasional paleosols. The lower part of this unit reflects a transition downhole in paleoenvironment from subaqueous to subaerial, marking the top of a significant interval of subaerial deposition in Unit 3.

The upper half of Unit 3 has a high proportion of coarse clastic sediments, with clasts including mafic/ultramafic lithologies, limestone, and chert (FA7; Subunit 3-1), that pass down into distinctive red-brown fine-grained muds and silts (FA8; Subunit 3-2; Figure F10). The very fine sand to mud fraction commonly contains abundant clay-sized Fe oxides that may be responsible for the reddish brown to pale yellow color of the sediments. The base of the unit (Subunit 3-3) comprises homogeneous muds of FA1 passing down into FA17 shelly bioturbated muds and sands. The character of the conglomerates and dominance of calcrete soils in Unit 3 suggest an ephemeral alluvial setting subject to a fluctuating water table.

Unit 4 at Site M0080 is dominated by shelly laminated to bedded carbonates (FA15 and FA16) that suggest a reduction in clastic input and most likely formed in a low-energy nearshore setting. The basal two cores of Unit 4 consist of polymict pebble-cobble conglomerates featuring abundant limestone clasts with minor red chert and mafic/ultramafic clasts, reflecting a high-energy alluvial (fan) environment.

Units 3 and 4 include ophiolitic-derived grains and clasts in all grain size fractions but most obviously in the coarser grain size range (sand to pebble grade). Carbonate minerals are most commonly calcite, whereas the ophiolitic-derived mafic/ultramafic sediment grains largely comprise pyroxenes, serpentinized olivine, and plagioclase.

Structural geology

Both natural and drilling-induced deformation were recorded in the cores. Natural faults were distinguished from drilling-induced faulting or other forms of drilling-induced deformation (DID) by their planar geometries and lack of influence by proximity to either the core liner or core axis (i.e., by not curving to become parallel to the core axis, forming conjugate pairs with an intersection at the core axis, or curving into the core liner). DID intensity and style were recorded to determine the state of cores for interpretation and analysis and for potential postexpedition analysis of sediment physical properties variations.

Site M0078

At Site M0078, bedding attitude is horizontal to subhorizontal with local tilting and apparent bedding dips increasing downhole to as high as 24° (slightly higher than estimated dips in coincident seismic reflection data; Figure F5). Small-scale natural faulting was observed sporadically throughout the hole, including frequent normal faults and less common strike-slip faults. Faulting intensity gener-

ally increases with depth but with faulting concentrated in discrete intervals, in particular in the 329.4–447.33 mbsf interval around the lithostratigraphic Unit 1/2 boundary. The apparent lack of faults in the deeper part of Unit 2 may be related to destruction by rotary drilling-induced biscuiting. Normal fault displacements range from 1 mm to 35 cm, and orientation measurements on selected faults indicate that they may form conjugate sets. The sampled normal fault dips show true dips ranging from 42° to 82° with a modal average of 60°–70° and a mean of 66°. The general abundance and geometry of observed small normal faults is in agreement with the overall extensional nature of the rift deformation.

A range of drilling-induced structures was observed, including biscuiting, arching bedding, tilted panels, lensing, smearing/flow of sediment along the core lining, voids, and open fractures. In general, DID increases downhole. Piston coring generated sporadic slight to moderate DID. Rotary coring from 224.34 mbsf downhole is associated with a marked increase in intensity (moderate to high) in DID, and deformation is dominated by biscuiting and inflow of sediment and drilling fluid between biscuits.

Site M0079

Bedding attitude is generally horizontal to subhorizontal despite a gentle increase in dip of reflection horizons with depth in seismic data at Site M0079 (Figure F6). Small-scale natural faulting was observed sporadically throughout the hole, and concentrated faulting was observed in discrete intervals at 48–62, 259–278, 472–548, and 686–698 mbsf. More significant faulting with larger displacements occurs below 547 mbsf. Faulting intensity varies downhole from 0.7 to 10 m⁻¹. All natural faults in Hole M0079A have apparent normal offset, with displacements of 1 mm to >14 cm. Faults sampled for orientation analysis appear to form a conjugate set around an average north-south strike in the core reference frame, but sampling is biased to surfaces that intersect the split-core face. The abundance and geometry of small normal faults are consistent with those observed at Site M0078 and with the extensional rift deformation.

A wide range of drilling-induced structures was observed, most commonly biscuiting, shear fractures, arching and disturbed bedding, smearing/flow of sediment along the edges of the core, voids, and open fractures; the intensity and style of drilling-induced structures vary downhole. Overall, DID intensity is markedly lower than in Hole M0078A (most likely due to changes in drilling and coring methods). Biscuiting is regularly present below 300 mbsf. Below 574 mbsf, cores are more intensely deformed, with biscuiting dominant. Well-developed, drilling-induced shear fracturing is a characteristic feature of Hole M0079A (not observed in Hole M0078A) and is a regular feature below 276 mbsf. Fractures often form as conjugate pairs typically intersecting in the center of the core or steepening toward the center of the core.

Site M0080

Bedding attitude is generally horizontal to subhorizontal, despite a gentle increase in dip of reflection horizons in seismic data at depth at Site M0080 (Figures F7, F10). Small-scale natural faulting was observed in lithostratigraphic Unit 1, Subunit 3-2, and Unit 4, with no faults between 101 and 368 mbsf (Unit 2 and Subunit 3-1). The lack of faulting in this interval may be related to lithologic and rheological properties. In Unit 1, faulting intensity varies from 1.4 to 10.5 m⁻¹, and all faults have apparent normal offsets with displacements of 0.2 mm to 3.2 cm. In Subunit 3-2 and Unit 4, faulting intensity varies from 0.7 to 4 m⁻¹. Some faults have apparent displacements larger than their length in the core and have fault

gouges and mineralized mirror surfaces with slickenlines. Faults sampled for orientation data illustrate a conjugate fault set striking NNE–SSW in the core reference frame in Unit 1, but sampling tends to be biased to surfaces that intersect the split-core face. In Subunit 3-2 and Unit 4, orientations are more variable, and slickenlines indicate oblique slip and strike-slip motion. The geometries of faults in Unit 1 are consistent with those at Sites M0078 and M0079 and the extensional rift deformation; however, the wider range of motion senses and geometries in Subunit 3-2 and Unit 4 suggest a more complex history of faulting here.

A wide range of drilling-induced structures was observed, most commonly biscuiting, shear fractures, arching bedding, smear-ing/flow of sediment along the edges of the core, and voids; the intensity and style of drilling-induced structures vary downhole. Significant lengths of core with little or no DID may be related to a combination of drilling technique and strength of the materials. Below 15 mbsf, DID associated with piston coring is pervasive with soupy textures, flow along the core liner and axis, and even complete mobilization and destruction of bedding in some cores. Biscuiting is dominant between 156 and 244 mbsf with the onset of rotary coring and again between 314 and 530 mbsf, where it is associated with intense brecciation between biscuits. Overall, shear fracturing is less common than at Site M0079.

Micropaleontology

Micropaleontological analysis included calcareous nannofossils, marine and nonmarine diatoms, planktonic and benthic foraminifers, and palynomorphs (terrestrial and aquatic pollen and spores, dinoflagellate cysts, green algae coenobia and spores, fungal remains, foraminifer test linings, and microscopic charred particles). The combined examination of microfossil groups in the youngest synrift sediments revealed variations between marine, mixed (marine with nonmarine), nonmarine, and indeterminate (e.g., barren) microfossil assemblages constructed by complex environmental and depositional settings in the Corinth basin; alternating paleoenvironment was particularly evident in the most recent rift phase. Each microfossil group contributes unique information to the regional/basinal paleoenvironmental interpretation. Additionally, calcareous nannofossils contributed to the chronostratigraphic model for the stratigraphic sequence. Diatoms provided critical information about depositional environments, especially in isolated intervals. Planktonic and benthic foraminifers were used to interpret the evolution of the paleoceanographic conditions in the basin during marine phases. Palynology provided a link between the terrestrial and aquatic realms and an assessment of changes in terrestrial paleovegetation and aquatic ecosystems.

Site M0078

The micropaleontology at Site M0078 revealed a high level of complexity both in individual microfossil groups and collectively. In the 16 subunits of lithostratigraphic Unit 1, micropaleontological assemblages alternate primarily between marine and undetermined assemblages but also include several mixed and nonmarine assemblages. Lithostratigraphic Unit 2 is devoid of marine calcareous and siliceous microfossils, containing only nonmarine diatoms and terrestrial and aquatic pollen, dinoflagellate cysts, green algae coenobia and spores, fungal remains, and foraminifer test linings. Calcareous nannofossils were observed in almost all Unit 1 samples but with significantly lower abundances and diversity in the isolated/semi-isolated subunits. In general, *Gephyrocapsa* is the most dominant genus. Late Quaternary age control in Unit 1 is provided

loosely by three biostratigraphic events: (1) the last occurrence (LO) of *Pseudoemiliana lacunosa* (0.43 Ma), supported by the co-occurrence with *Umbilicosphaera sibogae*; (2) the first occurrence (FO) of *Emiliana huxleyi* (0.29 Ma); and (3) a crossover in dominance between *E. huxleyi* and *Gephyrocapsa* “small” (<3 µm), documented to be ~70 ka in the Mediterranean Sea (Anthonissen and Ogg, 2012). Because of the punctuated nature of marine environments here, it is important to keep in mind that the depth precision of these biohorizons is low. Unit 2 is nearly devoid of in situ calcareous nannofossils. Marine diatoms were observed in the majority of the fully marine subunits. Nonmarine diatoms were most commonly observed in the isolated/semi-isolated subunits but were also sometimes observed in low abundance with marine microfossils where they were poorly preserved. The assemblages are not diverse and are dominated by species of the *Pontosphaera ocellata* group. The assemblages in the underlying Unit 2 are more diverse but are still dominated by the planktonic *P. ocellata* complex. Benthic and planktonic foraminifers are well preserved but have highly variable abundances and compositions in Unit 1. Foraminifers tend to be absent or in low abundances in isolated/semi-isolated subunits and abundant to trace in the marine subunits. In general, benthic foraminifers tend to be more abundant than planktonic foraminifers. Planktonic and benthic foraminifers are absent from Unit 2 samples. From palynological analysis, the trees versus herbs percentage curve shows alternating periods dominated by forests or herb vegetation that correlate with marine and isolated/semi-isolated intervals, respectively. The interpreted aquatic ecosystem ranges from marine to brackish to evidence for freshwater influx. Highly diverse marine dinoflagellate assemblages correlate with the fully marine intervals, and low dinocyst diversity samples with low salinity indicators suggest deposition under low-salinity (brackish) conditions.

Site M0079

The micropaleontology at Site M0079 revealed a high level of complexity both in individual microfossil groups and collectively, as at Site M0078. In the 16 subunits of lithostratigraphic Unit 1, micropaleontological assemblages alternate primarily between marine and undetermined assemblages but also include some mixed and nonmarine assemblages. Lithostratigraphic Unit 2 is nearly devoid of marine and terrestrial microfossils. Calcareous nannofossils were observed in almost all Unit 1 samples but with significantly lower abundances and diversity in isolated/semi-isolated subunits. *Gephyrocapsa* is the most dominant species. Late Quaternary age control in Unit 1 is provided loosely by the three biostratigraphic events that were also observed at Site M0078: (1) the LO of *P. lacunosa* (0.43 Ma), (2) the FO of *E. huxleyi* (0.29 Ma), and (3) a crossover in dominance between *E. huxleyi* and *Gephyrocapsa* “small” (<3 µm) (~70 ka). Because of the punctuated nature of marine environments here, it is important to bear in mind that the depth precision of these biohorizons is low. Unit 2 is completely devoid of in situ calcareous nannofossils. As at Site M0078, marine diatoms were observed in the majority of the fully marine subunits. Nonmarine diatoms were most commonly observed in the isolated/semi-isolated subunits, typically in combination with low abundances of marine microfossils. On occasion, nonmarine diatoms were observed in low abundance in marine intervals; however, because of poor preservation, they are not interpreted to be in situ. The nonmarine diatom assemblages are dominated by several morphotypes of the *P. ocellata* complex. Benthic and planktonic foraminifers are well preserved but have highly variable abundances and compositions in Unit 1. Eight intervals with relatively high abundances of

benthic and/or planktonic foraminifer species in Unit 1 suggest the prevalence of marine conditions. In these intervals, benthic foraminifer abundance is generally higher than that of planktonic foraminifers. Foraminifers tend to be absent or in low abundances in isolated/semi-isolated subunits, although intervals with higher foraminifer abundance were also observed. Planktonic and benthic foraminifers are absent from Unit 2 samples. The majority of the pollen assemblages corresponding to marine intervals in Unit 1 are characterized by high tree abundances, suggesting the occurrence of forested landscapes in the surroundings of the Gulf of Corinth, whereas in pollen assemblages corresponding to isolated/semi-isolated intervals, herb and tree abundances are nearly equal. As at Site M0078, dinoflagellate assemblages show alternating periods of marine and brackish paleoenvironments correlating with marine and isolated/semi-isolated intervals, respectively.

Site M0080

At Site M0080, the microfossil assemblages in lithostratigraphic Unit 1 indicate alternation primarily between marine and undetermined/barren assemblages but also include a few mixed and non-marine assemblages toward the base of the unit. Unit 2 alternates between nonmarine and undetermined/barren assemblages. Unit 3 is devoid of microfossils except palynomorphs because it is almost entirely terrestrial. Unit 4 is nearly devoid of the microfossil groups analyzed, with the exception of three samples that contain calcareous nannofossils in very low concentrations. Calcareous nannofossils similar to those observed at Sites M0078 and M0079 were observed in all marine intervals in Unit 1. Late Quaternary age control in Unit 1 is loosely provided by two biohorizons: (1) the crossover in dominance between *E. huxleyi* and *Gephyrocapsa* “small” (<3 µm) and (2) the FO of *E. huxleyi* (see Sites M0078 and M0079 for age details). As at Sites M0078 and M0079, the true FO of *E. huxleyi* was probably not observed. Units 2 and 3 are devoid of in situ calcareous nannofossils, and nannofossils are rarely present in Unit 4, where their implications for age are being investigated. Initial investigations suggest marine diatoms are present in significantly lower abundances than at Sites M0078 and M0079. The nonmarine diatom assemblages show better preservation and greater diversity of benthic taxa, indicating a shallower environment compared with the other two sites. Benthic and planktonic foraminifers are present only in Units 1 and 2, with highly variable abundances and compositions. Planktonic foraminifers similar to those observed at Sites M0078 and M0079 were observed in all marine intervals in Hole M0080A. The benthic foraminifer assemblages in the lower part of Unit 1 and in Unit 2 imply shallow-marine depositional environments. Pollen assemblages in Units 1 and 2 corresponding to interpreted marine intervals show high tree abundances, suggesting the occurrence of a forested landscape surrounding the Alkyonides Gulf, whereas in isolated/semi-isolated intervals, herb and tree abundances are nearly equal. Dinoflagellate assemblages indicating marine and brackish paleoenvironments were observed in Units 1 and 2, whereas Units 3 and 4 were devoid of dinocysts.

Geochemistry

Pore water was collected directly from cores offshore using Rhizons or squeeze cakes. Offshore, these samples were analyzed for alkalinity, ammonium (NH₄⁺), pH, and salinity. During the OSP, a combination of methods was applied to pore water samples to measure anions, cations, phosphate (PO₄³⁻), and dissolved inorganic carbon (DIC). Solid samples were selected and processed during the

OSP and were measured for X-ray fluorescence elemental composition, X-ray diffraction (results were incorporated into **Lithostratigraphy**), total carbon, and total organic carbon.

Site M0078

At Site M0078, 82 pore water samples were analyzed from Holes M0078A and M0078B, and 127 bulk sediment samples were processed during the OSP. Pore water and solid-phase chemical results follow very similar trends in Holes M0078A and M0078B. Pore water composition in the uppermost ~50 mbsf at Site M0078 reflects a diffusion profile of dissolved elements from the water column into the sediments (sodium [Na⁺], chloride [Cl⁻], and sulfate [SO₄²⁻]) and ions produced during the degradation of organic matter (NH₄⁺, bicarbonate [HCO₃⁻], PO₄³⁻, iron, and manganese). Comparison of salinity values with those of Na⁺ and Cl⁻ indicate that the major salt contributing to the pore water is NaCl. Significant changes between the pore water above and below the lithostratigraphic Unit 1/2 boundary were observed; higher concentrations of Na⁺ and Cl⁻ and ions associated with carbonates (calcium [Ca²⁺], magnesium [Mg²⁺], and strontium [Sr²⁺]) were observed below the boundary. Changes in pore water composition below the Unit 1/2 boundary may reflect the change in sediment composition, which is evident from the elemental composition of the solid sediment. Although solid sediment samples are carbonate rich throughout Hole M0078A, below the Unit 1/2 boundary an increase in the dominance of carbonate is clear from higher calcium concentrations. Organic carbon is low throughout Site M0078, ranging from 0.07 to 0.89 wt%.

Site M0079

At Site M0079, 77 pore water samples were analyzed, and 111 bulk sediment samples were processed during the OSP. From the seafloor to ~50 mbsf, pore water composition shows decreasing salinity (from 38.17 to 10.48) alongside decreasing pore fluid Na⁺, Cl⁻, and SO₄²⁻ concentrations. Dissolved Cl⁻ ranges between 7.82 and 610.49 mM, and Na⁺ varies from 51.65 to 541.73 mM; their highest values are in the upper 0.5 mbsf at the sediment/water interface.

Dissolved iron (Fe²⁺), which varies between 0.17 and 220.63 µM, and manganese, which ranges from <0.02 to 62.71 µM, both increase in the uppermost 8.65 mbsf, most likely due to generation of these ions during microbial oxidation of organic matter. Other ions generated during the degradation of organic matter (NH₄⁺, HCO₃⁻, and PO₄³⁻) also show this increase in the uppermost part of the hole but fluctuate with depth, reflecting the complex nature of the geochemical environment. Ions commonly associated with carbonates (Ca²⁺ [mean = 3.82 mM], Mg²⁺ [mean = 17.41 mM], and Sr²⁺ [mean = 0.11 mM]) also vary with depth and, similar to Hole M0078A, increase at the base of Hole M0079A. These observations are similar to solid phase results for these same elements.

Analysis of solid sediment samples (total inorganic carbon [TIC] and calcium) suggests that the sediment is predominantly composed of carbonate, which generally increases with depth (Ca = 175.0–228.0 g/kg; TIC = 3.95–10.52 wt%). Elements associated with detrital material (silicon, aluminum, zircon, and potassium), in contrast, decrease with depth.

Site M0080

At Site M0080, 62 pore water samples were analyzed, and 68 bulk sediment samples were processed during the OSP. Pore water profiles in the uppermost section of Hole M0080A show changes that most likely reflect diffusion profiles. Decreases in salinity from close to seawater values (35.74) to much lower values (12.38) at

49.45 mbsf, along with decreases in Na^+ , Cl^- and SO_4^{2-} concentrations, are likely linked to diffusion from seawater into the sediment. The highest concentrations of dissolved Fe^{2+} and manganese (as high as 166.74 and 31.45 μm , respectively) at the top of the hole decrease to relatively stable state concentrations deeper than ~30 mbsf. This trend is likely due to generation of these ions during oxidation of organic matter. Concentrations of other ions linked to organic matter degradation (NH_4^+ , PO_4^{3-} , alkalinity, and DIC) also increase in the uppermost ~20 mbsf (with maxima of 2.1 mM, 21.44 μM , 13.87 mM, and 12.59 mM, respectively). Deeper than ~20 mbsf, these ions continue to be present in variable concentrations, possibly relating to the loci of organic matter degradation.

Below the lithostratigraphic Unit 2/3 boundary, ions relating to organic matter degradation are generally present in low concentrations, whereas ions related to marine seawater appear to be high, comparable to modern day local seawater. Ca^{2+} and Mg^{2+} concentrations, which are typically related to carbonate, also increase in Unit 3. Average Ca^{2+} and Mg^{2+} concentrations are 8.16 and 38.86 mM, respectively, throughout the hole but reach maxima of 34.65 and 86.85 mM, respectively, in Unit 3.

Bulk geochemical results from solid sample analyses indicate that lithostratigraphic Units 1, 2, and 4 are dominated by calcium carbonate, with inorganic carbon averaging 8.34 wt% and calcium averaging 237.77 g/kg. In Unit 3, silicon dominates with an average of 172.68 g/kg compared with 83.63 g/kg in Units 1, 2, and 4. This switch in dominance, alongside higher values of aluminum, potassium, rubidium, and zirconium, suggests a change to more siliciclastic sediment in Unit 3, supported by lithostratigraphic interpretations (see [Lithostratigraphy](#)). Organic carbon content is low throughout, averaging 0.24 wt%, and is lowest in Unit 3 (average = 0.06 wt%).

Physical properties

Physical properties data acquired offshore and onshore on whole cores, split cores, and discrete samples exhibit coherent variations with depth and between different lithologies. Shear strength was estimated with handheld penetrometer measurements on whole cores and in situ cone penetration tests offshore and from fall cone and shear vane tests on split cores during the OSP. MSCL density data were acquired on whole cores offshore, and moisture and density (MAD) density and porosity were measured on discrete samples during the OSP. MSCL magnetic susceptibility, resistivity, and natural gamma radiation (NGR) data were acquired offshore on whole cores, and color reflectance data were acquired on split cores during the OSP. Attempts were made to collect *P*-wave velocity data on whole cores, half cores, and discrete samples. At Sites M0078 and M0079, reliable velocity measurements were only obtained in restricted intervals, primarily in the upper parts of the core, but reliable results were obtained for a large part of Site M0080. Between the offshore phase and the OSP, thermal conductivity measurements were conducted on whole cores prior to splitting.

Site M0078

At Site M0078, MAD, MSCL density, MSCL resistivity, and shear strength data indicate increases in sediment density and strength and a reduction in porosity with depth, consistent with compaction (Figure F8). Thermal conductivity also increases with depth. Sharp increases in density and shear strength were observed at 225 mbsf, near the transition to rotary coring. Overall, low NGR values at Site M0078 indicate low potassium (K), uranium (U), and thorium (Th) concentrations.

Physical properties vary between the two defined lithostratigraphic units and within Unit 1. In Unit 1, physical properties show clear variation between the marine and isolated/semi-isolated subunits. Marine subunits (odd numbers) are characterized by higher NGR values and lower and less scattered magnetic susceptibility values than isolated/semi-isolated subunits (even numbers; Figure F8). Lower density values are commonly associated with marine subunits and/or with transitions from these subunits into those above and below. Marine subunits have lower mean L^* and a^* values and higher mean b^* values compared with the means for the hole. Unit 2 is characterized by lower NGR values, scattered magnetic susceptibility values, and lighter colors, resulting in relatively higher mean L^* and a^* values and lower b^* values compared with Unit 1. Density values are less scattered in Unit 2 but show in-core trends in MSCL data related to coring and drilling.

Site M0079

Overall, as at Site M0078, MAD, MSCL density, MSCL resistivity, and shear strength data at Site M0079 indicate increases in sediment density and strength and a reduction in porosity with depth, consistent with compaction (Figure F9). However, low shear strength, density, and velocity values and high porosity values in the upper ~200 mbsf suggest relatively little compaction in this interval. Comparison between *P*-wave velocity values from discrete measurements, those from the downhole logging data, and those predicted by core-log-seismic integration (CLSI) suggests that velocity values from discrete core measurements in the upper ~225 mbsf are realistic but that velocity values are anomalously low deeper than ~225 mbsf.

Also similar to Hole M0078A, significant variations in Hole M0079A were observed in many physical properties between the marine and isolated/semi-isolated subunits in Unit 1, although some of these differences are less pronounced in Hole M0079A. Marine subunits tend to have higher NGR values and lower and less scattered magnetic susceptibility values than isolated/semi-isolated subunits (Figure F9). Lower density values are commonly associated with marine subunits and/or with transitions at the boundaries of these subunits. Conversely, shear strength and velocity appear to increase in some marine subunits. Some of the marine subunits have lower mean L^* and a^* values and higher mean b^* values compared with means for the hole from color reflectance data.

The lithostratigraphic Unit 1/2 boundary does not have a clear expression in physical properties measurements.

Site M0080

Physical properties from Hole M0080A cores show more variability than at Sites M0078 and M0079, reflecting the greater diversity of lithologies and depositional environments encountered. Most lithostratigraphic unit boundaries have a clear signature in the physical properties data. A change was also observed in the majority of physical properties data sets at the boundary between Subunits 3-1 and 3-2 at ~350 mbsf. Density values increase steadily with depth, consistent with compaction and strengthening (Figure F10). Resistivity shows slightly more complex variation with depth, with a pronounced increase in values downhole at the Unit 3/4 boundary.

Variations in physical properties reflecting environmental variation in Unit 1 were observed, as at Sites M0078 and M0079. In Unit 1, density and magnetic susceptibility increase and porosity and NGR decrease in isolated/semi-isolated intervals relative to the marine intervals. Marine subunits have lower mean L^* and a^* values and higher mean b^* values compared with means for the hole from

color reflectance data. Density, color reflectance, and porosity values become more scattered in the lower part of Unit 2 and transitioning into Unit 3. NGR decreases and then increases in Unit 3, followed by a sharp decrease into Unit 4 (Figure F10). Magnetic susceptibility increases in Unit 3, with a slight decrease with depth and a sharp reduction into Unit 4. These trends are thought to reflect the varied composition of the changing subaqueous and subaerial sequences in these units (see **Lithostratigraphy**).

Velocity data from discrete measurements in Units 1 and 2 are relatively low, but some values are consistent with sonic data acquired by downhole logging. In Units 3 and 4, both discrete and MSCL *P*-wave data appear to be more reliable. Velocity values average 2000 m/s in the lower part of Unit 3. Unit 4 is characterized by increased velocity values but with variations between the two core velocity data sets (discrete and MSCL).

Paleomagnetism

Site M0078

Magnetic susceptibility was measured on 501 discrete cubic samples from Holes M0078A and M0078B, and the results show a good match with MSCL magnetic susceptibility. Above ~300 mbsf, magnetic susceptibility variations are relatively small and exhibit different patterns in marine and isolated/semi-isolated subunits. Much higher variability in magnetic susceptibility was observed below ~300 mbsf. Overall, magnetic susceptibility and natural remanent magnetization (NRM) exhibit similar variations with depth, suggesting that susceptibility is primarily controlled by the concentration of magnetic minerals in the sediment.

Thermal variation of magnetic susceptibility was determined on five representative samples at the University of Hawaii prior to the OSP. Most samples show a primary Curie temperature of 518°–577°C, indicating the occurrence of Ti-poor titanomagnetite, although a couple of lower Curie temperatures were also identified and may indicate the additional occurrence of greigite.

The direction and intensity of NRM were determined on all samples from Holes M0078A and M0078B. The inclination values are dominantly positive (normal polarity) in Unit 1, which correspond to the Brunhes Normal Chron (0–0.773 Ma). Anomalously low inclination of the remanence of few samples from this uppermost interval may represent excursions of the geomagnetic field within the Brunhes Chron. Below the Unit 1–2 transition, inclination values are dominantly negative (reversed polarity), although several samples with normal polarity are also present. According to these data, the Brunhes/Matuyama boundary appears to be located at 385.99 mbsf, although both the occurrence and precise depth of this boundary remains highly speculative at this stage, and further postexpedition analysis will be needed.

Site M0079

Magnetic susceptibility was measured on 542 samples from Hole M0079A, and the results show a good match with MSCL magnetic susceptibility. Above ~540 mbsf, magnetic susceptibility variations are relatively small and exhibit different patterns in marine and isolated/semi-isolated subunits. Much higher variability in magnetic susceptibility was observed below ~540 mbsf. Overall, magnetic susceptibility and NRM exhibit similar variations with depth, suggesting that susceptibility is primarily controlled by the concentration of magnetic minerals in the sediment.

Thermal variation of magnetic susceptibility was determined on eight representative samples at the University of Hawaii prior to the

OSP. The results of the thermomagnetic experiments reveal a wide range of Curie temperatures between 364° and 595°C. However, most of the samples show a primary Curie temperature between 502° and 585°C, which is typical of Ti-poor titanomagnetite. Other Curie temperatures between 364° and 486°C suggest the additional occurrence of iron sulfides (likely greigite) or Ti-rich titanomagnetite.

The direction and intensity of NRM were determined on all samples from Hole M0079A. The inclination values are dominantly positive (normal polarity) in Unit 1, with the exception of two samples that show a negative inclination (reversed polarity). This uppermost normal polarity interval to 667.13 mbsf appears to correspond to the Brunhes Normal Chron (0–0.773 Ma), with the two reversed polarity samples possibly representing excursions of the geomagnetic field (Singer, 2014). The occurrence and precise depth of the Brunhes/Matuyama boundary and excursions at this stage remain highly speculative, and further postexpedition analyses will be needed. Furthermore, the inclination values show a wider variability from negative to positive below 667.13 mbsf throughout Unit 2, making the interpretation of the magnetostratigraphy for this interval challenging.

Site M0080

Magnetic susceptibility was measured on 379 samples from Hole M0080A, and the results show a good match with MSCL susceptibility. Above ~250 mbsf, magnetic susceptibility variations are relatively small. A much higher variability, with overall higher values of susceptibility, was observed between ~250 and ~460 mbsf, likely related to the occurrence of mafic ophiolitic clasts in Unit 3. Magnetic susceptibility and NRM exhibit similar variations with depth, suggesting that susceptibility is primarily controlled by the concentration of magnetic minerals in the sediment.

Thermal variation of magnetic susceptibility was determined on six representative samples at the University of Hawaii prior to the OSP. The results of the thermomagnetic experiments reveal a wide range of Curie temperatures between 116° and 646°C, indicating the occurrence of mixtures of Ti-rich titanomagnetite, iron sulfides (likely greigite), and likely oxidized titanomagnetite (i.e., titanomaghemite).

The direction and intensity of NRM were determined on 379 samples from Hole M0080A. The inclination values are dominantly positive (normal polarity) in Units 1 and 2 and the uppermost part of Unit 3, with six samples showing a negative inclination (reversed polarity). At greater depths, samples have a dominantly negative inclination (reversed polarity) that become positive again toward the bottom of the hole. The polarity transition observed in Unit 3 likely corresponds to the Brunhes/Matuyama boundary (0.773 Ma), and the reversed polarity intervals observed in the uppermost normal polarity interval may represent excursions of the geomagnetic field during the Brunhes Normal Chron. However, further postexpedition analyses are needed to confirm these hypotheses.

Downhole logging

Because of hole stability problems and the loss of tools in one hole, only partial logging of the three sites was conducted. At Site M0078, logging operations were conducted, but data are probably not usable. At Site M0079, a limited suite of logging tools was deployed, primarily in the upper ~295 m of the hole. At Site M0080, a full suite of standard logging tools was used to collect data through almost the entire borehole.

Site M0079

Downhole logging data were collected through the pipe (gamma ray) from the bottom of Hole M0079A to the seafloor and in the upper part of the open hole with logs recording magnetic susceptibility and conductivity (~297 to ~50 m wireline log depth below seafloor [WSF]), sonic velocity (~230 to ~50 m WSF), and dual resistivity (~290–50 m WSF). Gamma ray values, even though measured through the pipe, compare well with MSCL data collected on cores. The overall trend shows some correspondence to the marine and isolated/semi-isolated intervals. The slumped interval described in the deeper part of Unit 1 (484.48–506.40 mbsf; see **Lithostratigraphy**) is associated with a clear drop in gamma ray counts from the through pipe data. Resistivity values derived from the conductivity data (magnetic susceptibility and conductivity tool) and collected with the dual resistivity log compare well with each other and with MSCL resistivity data acquired on cores, and the values indicate low resistivity in the formation (typically <5 Ω m). Trends in the magnetic susceptibility log acquired downhole mirror those from MSCL data on cores, with a clear variation associated with changing basin environment: magnetic susceptibility tends to be lower in marine intervals/subunits and higher and more scattered in the isolated/semi-isolated intervals/subunits. Sonic data suggest low velocity, typically between 1500 and 1700 m/s from 50 to 190 m WSF and increasing to values as high as ~1900 m/s from 190 to 230 m WSF.

Site M0080

Hole M0080A logging operations were very successful, with most of the hole (0 to ~530 mbsf) covered with a suite of standard logging tools: spectral gamma ray through pipe and magnetic susceptibility and conductivity, dual induction resistivity, sonic, and spectral gamma ray in the open hole. Spectral gamma ray data were acquired through the pipe from the bottom of the hole to the seafloor and in the open hole principally from ~370 to 50 m WSF. Magnetic susceptibility and conductivity data cover most of the hole, with gaps from ~220 to ~230 m WSF and at 430 m WSF. Dual induction (resistivity) data cover the hole from ~370 to 50 m WSF, with a gap from ~220 to ~230 m WSF. Sonic data cover from the bottom of the hole to 50 m WSF, with gaps from ~430 to ~370 m WSF and from ~230 to ~220 m WSF.

The collected logs reflect the main lithostratigraphic units identified in Hole M0080A. In particular, magnetic susceptibility log data clearly respond to the changing depositional environments and sediment composition. Unit 1 is characterized by gamma ray counts of 50–100 counts/s, low magnetic susceptibility values, and relatively low velocity values between 1500 and 1600 m/s, consistent with some of the discrete velocity measurements. Gamma ray increases in marine subunits, and magnetic susceptibility shows locally higher values in the isolated/semi-isolated subunits of Unit 1. In Unit 2, the gamma ray counts are lower than in Unit 1 and magnetic susceptibility remains low with local increases in Subunits 2-4 and 2-5. Velocity values increase to 1700–2000 m/s in Unit 2. Magnetic susceptibility increases significantly in Unit 3, associated with increased scattering, and then progressively decreases downhole in Units 3 and 4. Similar scattering was observed in the resistivity data. Sonic velocity increases to values >2000 m/s. Data in this unit may be affected by poorer and variable borehole conditions. At the boundary between Subunits 3-1 and 3-2, magnetic susceptibility decreases, gamma ray increases, and resistivity and sonic velocity sharply increase. In Unit 4, gamma ray (through pipe) drops to its lowest values, magnetic susceptibility remains low with little varia-

tion, and sonic velocity increases abruptly to values close to 3000 m/s.

Velocity data acquired on whole-round cores (MSCL) and discrete samples and from downhole logs show similar trends, but values differ slightly in some parts of the hole. In particular, in the deeper part of the hole (Unit 4) MSCL data indicate velocity values that are ~500–1000 m/s slower than sonic velocity values, and discrete core measurement values sit between these two data sets.

Core-log-seismic integration

The goal of CLSI during Expedition 381 was to tie data and observations from each of the sites to the extensive seismic reflection database available in the Gulf of Corinth (e.g., Sachpazi et al., 2003; Zelt et al., 2004; Taylor et al., 2011; McNeill et al., 2005; Bell et al., 2008, 2009; Lykousis et al., 2007; Sakellariou et al., 2007; Collier et al., 2000; Leeder et al., 2002, 2005; Stefatos et al., 2002; Charalampakis et al., 2014; Nixon et al., 2016) (e.g., Figure F3). Synthetic seismograms were calculated with MSCL and MAD density and, where available, with velocity information from downhole logging, core physical properties, or existing pre-expedition velocity profiles derived from seismic data.

Site M0078

Synthetic seismograms for Site M0078 (Figure F5) were calculated from MSCL density data from Holes M0078A and M0078B and a linear velocity function estimated from seismic data before the expedition. Unfortunately, neither core MSCL nor discrete V_p measurements produced reliable velocity data for Site M0078, and no downhole logging data were collected. Nonetheless, the synthetic seismograms can be reliably tied to the seismic data using the pre-expedition velocity function. Minor adjustments to the velocity function were made to match prominent reflections in the synthetic seismogram to those in the coincident seismic data. Above 250 mbsf, the main high-reflectivity horizons in lithostratigraphic Unit 1 (seismic Unit 2) correspond to marine subunits, confirming the interpretations of Nixon et al. (2016) and other previous authors. However, the marine intervals are sometimes thinner than estimated from the reflection data prior to the expedition. In the lower part of Unit 1 (below ~250 mbsf), correlating seismic reflectors with subunit boundaries becomes more challenging because this part of the section is condensed and parts of the section may be missing. In this depth range, observed marine and isolated/semi-isolated subunits sometimes correspond to the seismic phases but sometimes differ. The lower reflectivity sequences of lithostratigraphic Unit 2 (seismic Unit 1; Figure F5) proved to be more challenging to match to seismic reflection data because of the lack of impedance contrasts in the core and seismic records. However, at least two low-reflectivity horizons in Unit 2 can be potentially traced in the synthetic seismogram and tied to seismic data.

Site M0079

MSCL density data were combined with an integrated velocity function to calculate synthetic seismograms at Site M0079. The velocity function was created from discrete velocity values and sonic data from downhole logging in the upper part of Hole M0079A and a velocity function based on preliminary offshore CLSI in the lower part of the hole, where other velocity data were not available. A comparison of all available velocity information indicates that the upper ~200 mbsf is characterized by relatively low velocity values that suggest limited compaction, consistent with other physical properties. Further minor adjustments to the velocity function were

made to match prominent reflections in the synthetic seismogram to those in the coincident seismic data. Synthetic seismograms exhibit patterns of high and low reflectivity similar to those observed in seismic data crossing the site (Figure F6). Intervals of high reflectivity in synthetic seismograms correspond to marine subunits from lithostratigraphic Unit 1, confirming the interpretations of Nixon et al. (2016) and previous authors. In detail, CLSI demonstrates that the tops of marine intervals correspond to the onsets of high-reflectivity intervals. In the lower part of Unit 1, the relationship between bright reflections and marine subunits is more complex, likely owing to the small thicknesses of marine subunits in this part of the hole. The deepest reflection, interpreted to be the unit boundary in seismic data, may in fact correspond to the deepest marine interval in lithostratigraphic Unit 1.

Site M0080

For Site M0080, MSCL density data were combined with a velocity function created from discrete velocity values, sonic data from downhole logging, and velocity values from offshore MSCL data to calculate synthetic seismograms. A comparison of all available velocity information indicates that the upper ~140 mbsf is characterized by relatively low velocity values that suggest limited compaction, consistent with other physical properties. From ~150 to ~450 mbsf, an increase in velocity corresponds, on average, to the velocity function estimated from seismic data before the expedition. Below ~450 mbsf, a significant difference in average MSCL velocity values and the downhole logging velocity values occurs, with the former suggesting a lower range of ~2000–2500 m/s and the latter varying from ~2500 to 3500 m/s. Both velocity scenarios were utilized for synthetic seismogram generation to determine sensitivity to uncertainty in the input velocity profile.

Synthetic seismograms at Site M0080 match the coincident seismic data remarkably well. The four lithostratigraphic units identified from the cores have visibly different expressions in the seismic data around the site (Figure F7). Lithostratigraphic Unit 1, a succession of relatively thin marine and isolated/semi-isolated subunits, exhibits a series of continuous reflectors with a very pronounced positive phase, likely produced by the change to lower density in the marine intervals. Select subunit boundaries can be reliably traced from the cores to the seismic data. Lithostratigraphic Unit 2 is characterized by a series of continuous reflectors with equally pronounced positive and negative phases. Lithostratigraphic Unit 3 has a more complex reflectivity signature characterized by discontinuous reflectors and some gaps in reflectivity, corresponding to the conglomerates in Subunit 3-1 and potential faults at the base of Subunit 3-2.

Below ~450 mbsf, the synthetic seismogram and its correlation with lithostratigraphic Unit 4 varies significantly depending on the input velocity model, making correlations significantly more uncertain. For the case of lower input velocity values derived from MSCL data, the top and bottom of Unit 4 are marked by two distinct reflectors, the shallower of which was previously attributed to the top of acoustic basement (Nixon et al., 2016) but could now be interpreted to be the transition into basal conglomerates. Alternatively, using the higher velocity values derived from the downhole log data, the whole of Unit 4 maps onto the upper of these two reflectors, and subunit boundaries in Unit 4 cannot be resolved. In this case, the reflector interpreted to be the top of acoustic basement would be intersected at the very bottom of Hole M0080A. Based on the properties of the cored materials, the latter interpretation is favored, but further work will be required to distinguish between these two end-members.

Preliminary scientific assessment

The overarching objective of Expedition 381 was to drill, sample, and analyze the synrift sedimentary sequence that records an extended period of the early stage continental rifting process in the Corinth rift, Greece. This is the first time a record of this length and resolution has been recovered in an active rift system. In the Corinth rift, part of the rift depositional record is preserved onshore, but the most recent sequence is only present offshore. Onshore, only limited dating of the sedimentary sequence has been possible; therefore, there is little constraint on timing and rates of geological processes. Obtaining this new drilled record will make it possible to develop the chronostratigraphy, determine the environment of the basin through its rift development history, quantify changes in depositional processes and sediment flux in the basin, and determine the rates and timings of rift and fault development, fault slip, and fault activity history.

Expedition 381 was extremely successful. The drilling and coring objectives were almost completely achieved, and a total of 1645 m of core was recovered from three sites over a 1905 m cored interval. At Site M0078, the borehole depth was shortened slightly because of projected time constraints; therefore, an intended part of the older synrift section was not recovered. At Site M0080, the drilling target was to reach acoustic basement (the older sedimentary sequences underlying the synrift sequence). Basal conglomerates interpreted to immediately overlie basement were recovered, but insufficient time remained to continue to basement itself. Because of hole stability problems and the loss of tools in one hole, only partial logging of the three sites was conducted. At Site M0078, logging operations were conducted, but data are probably not usable. At Site M0079, a limited suite of logging tools was deployed, primarily in the upper ~295 m of the hole. At Site M0080, a full suite of standard logging tools was used to collect data through almost the entire borehole. In spite of these (relatively minor) changes to the operational program, the combined coring and logging data sets collected will fully enable us to address the objectives of the expedition. Core recovery was excellent (average = 86%), and core quality is good overall. Changes to coring and drilling methods during the expedition significantly improved subsequent core quality and increased rates of progress, enabling the three sites to be completed very nearly as planned in the time available.

The potential range of scientific applications for this unique data set is very large, encompassing tectonics, sedimentary processes, paleoenvironment, paleoclimate, paleoecology, geochemistry, and geohazards. We anticipate exciting and important results from both the postexpedition research and from research endeavors beyond the science party for many years to come.

Active rift sedimentary processes

The three drill sites of Expedition 381 capture a long and high-resolution record of sedimentation in the center of the Gulf of Corinth and Alkyonides Gulf, with primarily fine grained, distal sediment gravity flow and hemipelagic deposits. The core materials show a clear link to the changing environment of the basin in the most recent synrift succession, namely an alternation between a marine environment during global sea level highstands and an isolated/semi-isolated environment during global sea level lowstands (Unit 1). In the marine intervals, sediments are predominantly homogeneous bioturbated muddy sediments with a marine biogenic assemblage. In the isolated/semi-isolated intervals, sediments tend to exhibit clearer bedding and fine-scale lamination, with coarser

laminations and beds apparently more pronounced. Sediment composition, primarily carbonate, shows a clear correlation with onshore drainage basins and sediment sources, and grain analyses will be used in postexpedition research to assess changes in provenance. Organic components are common in the sediments, possibly with both marine and terrestrial sources, and these components in turn affect the geochemistry of the sediments and pore waters. In the deeper and older rift sequences of the sites in the central gulf (Unit 2; Sites M0078 and M0079; Figure F1), sediments become more homogeneous and lack the clear cyclical signature related to the changing environment of the basin driven by global sea level, as seen in the overlying sequence. Slump and debris flow deposits appear to be more common at depth in the sequence, in particular at Site M0079, and may reflect a change in rift faulting activity and/or sediment flux.

In the Alkyonides Gulf at Site M0080 (Figure F1), the sedimentary sequence is more variable than at sites in the central gulf (Sites M0078 and M0079). These differences may reflect the smaller drainage systems feeding the basin, the shallower water depth of the site, closer proximity to the shoreline, and/or greater variability of onshore basement lithology. At depth at Site M0080, terrestrial alluvial–fluvial sequences and deposits indicative of a shallow ephemeral basin fluctuating between a subaqueous and subaerial environment are preserved. These deposits predate the most recent phase of deeper water deposition affected by changing global sea level. The exact age of these older deposits is not yet clear, but they may include a record of an earlier phase of Corinth rifting than that penetrated by the boreholes in the central gulf (Sites M0078 and M0079). Correlation of the earliest deposits at all three sites with the onshore exhumed synrift sequences will be a crucial element of postexpedition research to generate a complete history of Corinth rift evolution and deposition and to identify any along-axis variations in rift evolutionary history.

Paleoenvironment of the Corinth rift basin

Sediments from the most recent rift phase reveal substantial temporal variations in paleoenvironment in the Gulf of Corinth that appear to be controlled by sea level fluctuations with respect to the topographic sills bounding this semi-isolated basin and the supply of riverine water to the basin (McNeill et al., submitted). These changes are manifest in varying microfossil assemblages, sediment lithology, physical properties, and the chemistry of the basin sediments and pore fluids. During marine periods when the gulf was connected to the global oceans, typical assemblages of marine microfossils were observed, including combinations of benthic and planktonic foraminifers, marine diatoms, calcareous nannofossils, and marine dinoflagellate cysts; however, the abundance and diversity of microfossil groups vary between sites and with time. During isolated/semi-isolated periods when the gulf appears to have been fully or partially cut off from the global ocean, microfossil assemblages are often complex, suggesting multifaceted paleoenvironmental conditions. The transitions between the marine and isolated/semi-isolated intervals expressed in the micropaleontological and sedimentary record are particularly complex and varied in their length and character. Pollen analysis of the deposits also provides a link between the terrestrial and aquatic environments. The sea level–driven paleoenvironmental change in the late Quaternary basin is also recorded in the lithology and geochemistry of the most recent synrift sediments. The volume and mode of sediment delivery into the rift basin appear to change between marine and isolated/semi-isolated intervals (McNeill et al.,

submitted). Variations in the geochemistry of the sediments and pore fluids were also observed over this part of the drilled interval, with apparent links to the paleoenvironmental changes (C.M. Miller et al., unpubl. data).

At greater depths in the boreholes, older parts of the synrift sedimentary fill (Unit 2; Sites M0078 and M0079) appear to be dominantly nonmarine, suggesting that at least the central gulf was primarily isolated during this earlier phase. Although extended intervals are devoid of microfossils, likely as a result of poor preservation (e.g., dissolution, scavenging, etc.), significant bioturbation was observed; therefore, the environmental conditions in these periods are less clear. In the Alkyonides Gulf of the eastern rift (Site M0080), the recovered synrift sediments from earlier phases of basin development indicate both terrestrial and subaqueous conditions.

Further postexpedition research and integration of micropaleontological, sedimentological, and geochemical observations and analyses will be needed to more fully understand the complex changes in paleoenvironment over the history of the Corinth rift and how these changes relate to its tectonic and climatic evolution and its connectivity to the Mediterranean. Comparisons with other basins with varying paleoenvironments, such as the Sea of Marmara and the Black Sea, will form part of this process. The Corinth rift cores will also provide a new, long Quaternary record of Mediterranean-type climate in the region, complementing long records farther north in the southern Balkans–Greece, such as from Lake Ohrid, Lake Kopais, Lake Ioannina, Tenaghi Philippon (e.g., Tzedakis et al., 2009; Sadori et al., 2016), and elsewhere in the Mediterranean Sea.

Chronostratigraphy

One of the primary objectives of Expedition 381 was to obtain age constraints on synrift sediments that can be used to quantify rates of tectonic and sedimentary processes at high temporal resolution in this young and active rift. Shipboard characterization of the recovered cores indicates that this objective will be achievable by using a suite of complementary dating and paleoenvironmental characterization methods, although this process will take time and will be challenging. Shipboard analyses have already yielded important age constraints that will be greatly expanded by postexpedition research efforts.

Shipboard efforts included biostratigraphy, magnetostratigraphy, and, less directly, identification of alternating basin conditions linked to past sea level fluctuations and glacial–interglacial cycles (McNeill et al., submitted). Two key calcareous nannofossil markers were observed in the sedimentary record of the most recent rifting phase: *E. huxleyi* (FO at 0.29 Ma) and *P. lacunosa* (LO at 0.43 Ma). However, because the basin alternates between marine and isolated conditions and thus does not possess a continuous record of marine microfossils, interpreting these biohorizons must be undertaken with care. Magnetostratigraphy provides baseline chronological ties for the drilled section, including probable identification of the Brunhes/Matuyama boundary at all sites and potential correlations with other earlier chrons. With further postexpedition research, the opportunity to identify excursions of the geomagnetic field and to develop and correlate with the global RPI record should further improve the resolution of the chronostratigraphy. Finally, pinpointing changes in basin paleoenvironment linked to glacial–interglacial cycles also provides indirect age constraints. These data indicate that the most recent phase of rift deformation is late Quaternary and that pre-expedition correlations with glacial–interglacial cycles are broadly correct. The

penultimate phase of rift deformation also appears to be Quaternary in age, but further analysis is required to pinpoint ages more precisely and to examine any spatial variations in rift history.

The cores clearly contain a rich trove of material that can be used to provide further age constraints. To develop a final age model for each site, shipboard results will be complemented by a series of postexpedition research efforts, including radiocarbon dating of the youngest sediments, stable isotope analyses from the marine intervals, magnetic RPI, and tephrochronology. The results will be crucial for studies of rift evolution, sedimentary processes, and paleoenvironment.

Structure and deformation

The three drill sites were purposely located away from major seismic-scale faulting to maximize recovery of a complete stratigraphic sequence and to avoid the challenges of drilling through faults. However, small-scale conjugate normal faulting, compatible with the present-day extensional regime, was observed in the cored sequence at all three sites.

Faults are also common in the deeper part of Site M0080 in the Alkyonides Gulf of the eastern Corinth rift where they record a more complex deformation history that reflects the probable longer sedimentary record captured here. Quantification of the core-scale structures and their integration with seismic-scale structures imaged throughout the extensive seismic reflection database will contribute toward characterizing subseismic strain in an active rift environment. This is an elusive but significant parameter for reliably calculating strain and for estimating the integrity of petroleum reservoirs and traps.

Rift evolution

Expedition 381 objectives on rift evolution will be principally achieved during postexpedition research. Postexpedition analyses will build on the shipboard analyses to develop a high-resolution chronology for the synrift sequence sampled (e.g., biostratigraphy, tephrochronology, magnetostratigraphy, magnetic RPI, radiocarbon, and stable and radiogenic isotopes). Core and log velocity and density data will be the basis for improved CLSI, enabling correlation of the drill cores with the extensive seismic data set, in particular increasing the precision of seismic reflector ties and time-depth conversion. These new sedimentary, physical properties, and chronological data sets will be used to provide considerably improved constraints on ages of synrift seismic stratigraphic horizons and hence fault displacements, sediment thicknesses, volumes and compaction history, and the timing of major rift events. Thus, we will be able to determine rift fault activity and slip rates in space and time, including in the very recent past for the purposes of hazard assessment, the timing and rate of development of the rift fault network, and the longer term rift evolution, including discrete rift phases and changes in rates of extension and subsidence. Analysis of the stratigraphic sequence, including sediment provenance and calculation of sediment fluxes in space and time, and its integration and correlation with the onshore elements of the rift sequence will allow for building a model of rift basin and sedimentary development. By tying these data with existing data and new data from drilling on the regional paleoclimate and vegetation cover and the paleoenvironment of the basin, the relative roles of climate, tectonics, and sea level/water depth on sediment flux into the basin and the history of basin filling can be unraveled (see preliminary results in McNeill et al., submitted). The integration of drilling data, seis-

mic network, and preserved sequences onshore will provide a unique opportunity to model the temporal and 3-D spatial tectonic and sedimentological development of a young rift basin.

References

- Andrews, J.E., Portman, C., Rowe, P.J., Leeder, M.R., and Kramers, J.D., 2007. Sub-orbital sea-level change in early MIS 5e: new evidence from the Gulf of Corinth, Greece. *Earth and Planetary Science Letters*, 259(3–4):457–468. <https://doi.org/10.1016/j.epsl.2007.05.005>
- Anthonissen, D.E., and Ogg, J.G., 2012. Appendix 3—Cenozoic and Cretaceous biochronology of planktonic foraminifera and calcareous nannofossils. In Gradstein, F.M., Ogg, J.G., Schmitz, M.D., and Ogg, G.M., (Eds.), *The Geologic Time Scale 2012*: Amsterdam (Elsevier), 1083–1127. <https://doi.org/10.1016/B978-0-444-59425-9.15003-6>
- Armijo, R., Meyer, B., King, G.C.P., Rigo, A., and Papanastassiou, D., 1996. Quaternary evolution of the Corinth Rift and its implications for the Late Cenozoic evolution of the Aegean. *Geophysical Journal International*, 126(1):11–53. <https://doi.org/10.1111/j.1365-246X.1996.tb05264.x>
- Avallone, A., Briole, P., Agatza-Balodimou, A.M., Billiris, H., Charade, O., Mitsakaki, C., Nercessian, A., Papazissi, K., Paradissis, D., and Veis, G., 2004. Analysis of eleven years of deformation measured by GPS in the Corinth Rift Laboratory area. *Comptes Rendus Geosciences*, 336(4–5):301–311. <https://doi.org/10.1016/j.crte.2003.12.007>
- Backert, N., Ford, M., and Malartre, F., 2010. Architecture and sedimentology of the Kerinitis Gilbert-type fan delta, Corinth Rift, Greece. *Sedimentology*, 57(2):543–586. <https://doi.org/10.1111/j.1365-3091.2009.01105.x>
- Bayrakci, G., Minshull, T.A., Sawyer, D.S., Reston, T.J., Klaeschen, D., Papenberg, C., Ranero, C., et al., 2016. Fault-controlled hydration of the upper mantle during continental rifting. *Nature Geoscience*, 9(5):384–388. <https://doi.org/10.1038/ngeo2671>
- Bell, R.E., McNeill, L.C., Bull, J.M., and Henstock, T.J., 2008. Evolution of the offshore western Gulf of Corinth. *Geological Society of America Bulletin*, 120(1–2):156–178. <https://doi.org/10.1130/B26212.1>
- Bell, R.E., McNeill, L.C., Bull, J.M., Henstock, T.J., Collier, R.E.L., and Leeder, M.R., 2009. Fault architecture, basin structure and evolution of the Gulf of Corinth Rift, central Greece. *Basin Research*, 21(6):824–855. <https://doi.org/10.1111/j.1365-2117.2009.00401.x>
- Bell, R.E., McNeill, L.C., Henstock, T.J., and Bull, J.M., 2011. Comparing extension on multiple and depth scales in the Corinth Rift, central Greece. *Geophysical Journal International*, 186(2):463–470. <https://doi.org/10.1111/j.1365-246X.2011.05077.x>
- Bentham, P., Collier, R.E., Gawthorpe, R.L., Leeder, R., and Stark, C., 1991. Tectono-sedimentary development of an extensional basin: the Neogene Megara Basin, Greece. *Journal of the Geological Society*, 148(5):923–934. <https://doi.org/10.1144/gsjgs.148.5.0923>
- Bernard, P., Lyon-Caen, H., Briole, P., Deschamps, A., Boudin, F., Makropoulos, K., Papadimitriou, P., et al., 2006. Seismicity, deformation and seismic hazard in the western rift of Corinth: new insights from the Corinth Rift Laboratory (CRL). *Tectonophysics*, 426(1–2):7–30. <https://doi.org/10.1016/j.tecto.2006.02.012>
- Bialas, R.W., and Buck, W.R., 2009. How sediment promotes narrow rifting: application to the Gulf of California. *Tectonics*, 28(4):TC4014. <https://doi.org/10.1029/2008TC002394>
- Briole, P., Rigo, A., Lyon-Caen, H., Ruegg, J.C., Papazissi, K., Mitsakaki, C., Balodimou, A., Veis, G., Hatzfeld, D., and Deschamps, A., 2000. Active deformation of the Corinth Rift, Greece: results from repeated global positioning system surveys between 1990 and 1995. *Journal of Geophysical Research: Solid Earth*, 105(B11):25605–25625. <https://doi.org/10.1029/2000JB900148>
- Burov, E., and Poliakov, A., 2001. Erosion and rheology controls on synrift and postrift evolution: verifying old and new ideas using a fully coupled numerical model. *Journal of Geophysical Research: Solid Earth*, 106(B8):16461–16481. <https://doi.org/10.1029/2001JB000433>
- Capotondi, L., Girone, A., Lirer, F., Bergami, C., Verducci, M., Vallefucio, M., Afferri, A., Ferraro, L., Pelosi, N., and De Lange, G.J., 2016. Central Medi-

- terranean mid-Pleistocene paleoclimatic variability and its association with global climate. *Palaeogeography, Palaeoclimatology, Palaeoecology*, 442:72–83. <https://doi.org/10.1016/j.palaeo.2015.11.009>
- Channell, J.E.T., Hodell, D.A., Xuan, C., Mazaud, A., and Stoner, J.S., 2008. Age calibrated relative paleointensity for the last 1.5 Myr at IODP Site U1308 (North Atlantic). *Earth and Planetary Science Letters*, 274(1–2):59–71. <https://doi.org/10.1016/j.epsl.2008.07.005>
- Channell, J.E.T., Xuan, C., and Hodell, D.A., 2009. Stacking paleointensity and oxygen isotope data for the last 1.5 Myr (PISO-1500). *Earth and Planetary Science Letters*, 283(1–4):14–23. <https://doi.org/10.1016/j.epsl.2009.03.012>
- Charalampakis, M., Lykousis, V., Sakellariou, D., Papatheodorou, G., and Ferentinos, G., 2014. The tectono-sedimentary evolution of the Lechaion Gulf, the south eastern branch of the Corinth graben, Greece. *Marine Geology*, 351:58–75. <https://doi.org/10.1016/j.margeo.2014.03.014>
- Cita, M.B., Vergnaud-Grazzini, C., Robert, C., Chamley, H., Ciaranfi, N., and d'Onofrio, S., 1977. Paleoclimatic record of a long deep sea core from the eastern Mediterranean. *Quaternary Research*, 8(2):205–235. [https://doi.org/10.1016/0033-5894\(77\)90046-1](https://doi.org/10.1016/0033-5894(77)90046-1)
- Clarke, P.J., Davies, R.R., England, P.C., Parson, B., Billiris, H., Paradissis, D., Veis, G., et al., 1998. Crustal strain in central Greece from repeated GPS measurements in the interval 1989–1997. *Geophysical Journal International*, 135(1):195–214. <https://doi.org/10.1046/j.1365-246X.1998.00633.x>
- Collier, R.E.L., Leeder, M.R., Trout, M., Ferentinos, G., Lyberis, E., and Papatheodorou, G., 2000. High sediment yields and cool, wet winters: test of last glacial paleoclimates in the northern Mediterranean. *Geology*, 28(11):999–1002. [https://doi.org/10.1130/0091-7613\(2000\)28<999:HSYACW>2.0.CO;2](https://doi.org/10.1130/0091-7613(2000)28<999:HSYACW>2.0.CO;2)
- Ford, M., Hemelsdaël, R., Mancini, M., and Palyvos, N., 2016. Rift migration and lateral propagation: evolution of normal faults and sediment-routing systems of the western Corinth rift (Greece). In Childs, C., Holdsworth, R.E., Jackson, C.A.-L., Manzocchi, T., Walsh, J.J., and Yielding, G. (Eds.), *The Geometry and Growth of Normal Faults*. Geological Society Special Publication, 439:131–168. <https://doi.org/10.1144/SP439.15>
- Ford, M., Rohais, S., Williams, E.A., Bourlange, S., Jousset, D., Backert, N., and Malartre, F., 2013. Tectono-sedimentary evolution of the western Corinth Rift (central Greece). *Basin Research*, 25(1):3–25. <https://doi.org/10.1111/j.1365-2117.2012.00550.x>
- Ford, M., Williams, E.A., Malartre, F., and Popescu, S.-M., 2007. Stratigraphic architecture, sedimentology and structure of the Vouraikos Gilbert-type fan delta, Gulf of Corinth, Greece. In Nichols, G., Paola, C., and Williams, E. (Eds.), *Sedimentary Processes, Environments and Basins: A Tribute to Peter Friend*. Jarvis, I. (Series Ed.). Special Publication of the International Association of Sedimentologists, 38:44–90. <https://doi.org/10.1002/9781444304411.ch4>
- Gawthorpe, R.L., Jackson, C.A.-L., Young, M.J., Sharp, I.R., Moustafa, A.R., and Leppard, C.W., 2003. Normal fault growth, displacement localisation and the evolution of normal fault populations: the Hammam Faraou fault block, Suez Rift, Egypt. *Journal of Structural Geology*, 25(6):883–895. [https://doi.org/10.1016/S0191-8141\(02\)00088-3](https://doi.org/10.1016/S0191-8141(02)00088-3)
- Gawthorpe, R.L., and Leeder, M.R., 2000. Tectono-sedimentary evolution of active extensional basins. *Basin Research*, 12(3–4):195–218. <https://doi.org/10.1111/j.1365-2117.2000.00121.x>
- Gawthorpe, R.L., Leeder, M.R., Haralambos, K., Skourtsos, E., Andrews, J.E., Henstra, G.A., Mack, G.H., Muravchik, M., Turner, J.A., and Stamatakis, M., 2017. Tectono-sedimentary evolution of the Plio–Pleistocene Corinth rift, Greece. *Basin Research*. <https://doi.org/10.1111/bre.12260>
- Heezen, B.C., Ewing, M., and Johnson, G.L., 1966. The Gulf of Corinth floor. *Deep Sea Research and Oceanographic Abstracts*, 13(3):381–411. [https://doi.org/10.1016/0011-7471\(66\)91076-X](https://doi.org/10.1016/0011-7471(66)91076-X)
- Hemelsdaël, R., Ford, M., Malartre, F., and Gawthorpe, R., 2017. Interaction of an antecedent fluvial system with early normal fault growth: implications for syn-rift stratigraphy, western Corinth rift (Greece). *Sedimentology*, 64(7):1957–1997. <https://doi.org/10.1111/sed.12381>
- Higgs, B., 1988. Syn-sedimentary structural controls on basin deformation in the Gulf of Corinth, Greece. *Basin Research*, 1(3):155–165. <https://doi.org/10.1111/j.1365-2117.1988.tb00012.x>
- Huisman, R.S., and Beaumont, C., 2007. Roles of lithospheric strain softening and heterogeneity in determining the geometry of rifts and continental margins. *Geological Society Special Publications*, 282(1):111–138. <https://doi.org/10.1144/SP282.6>
- Huisman, R., and Beaumont, C., 2011. Depth-dependent extension, two-stage breakup and cratonic underplating at rifted margins. *Nature*, 473(7345):74–78. <https://doi.org/10.1038/nature09988>
- Jolivet, L., 2001. A comparison of geodetic and finite strain pattern in the Aegean, geodynamic implications. *Earth and Planetary Science Letters*, 187(1–2):95–104. [https://doi.org/10.1016/S0012-821X\(01\)00277-1](https://doi.org/10.1016/S0012-821X(01)00277-1)
- Jolivet, L., Brun, J.-P., Gautier, P., Lallament, S., and Patria, M., 1994. 3D-kinematics of extension in the Aegean region from the early Miocene to the present: insights from the ductile crust. *Bulletin de la Société Géologique de France*, 165(3):195–209. <http://bsgf.geoscienceworld.org/content/gssgfbull/165/3/195.full.pdf>
- Jolivet, L., Labrousse, L., Agard, P., Lacombe, O., Bailly, V., Lecomte, E., Mouthereau, F., and Mehl, C., 2010. Rifting and shallow-dipping detachments, clues from the Corinth Rift and the Aegean. *Tectonophysics*, 483(3–4):287–304. <https://doi.org/10.1016/j.tecto.2009.11.001>
- Lavier, L.L., and Buck, W.R., 2002. Half graben versus large-offset low-angle normal fault: importance of keeping cool during normal faulting. *Journal of Geophysical Research: Solid Earth*, 107(B6):ETG 8-1–ETG 8-13. <https://doi.org/10.1029/2001JB000513>
- Lavier, L.L., and Manatschal, G., 2006. A mechanism to thin the continental lithosphere at magma-poor margins. *Nature*, 440(7082):324–328. <https://doi.org/10.1038/nature04608>
- Le Pichon, X., and Angelier, J., 1981. The Aegean Sea. *Philosophical Transactions of the Royal Society, A: Mathematical, Physical & Engineering Sciences*, 300(1454):357–372. <https://doi.org/10.1098/rsta.1981.0069>
- Leeder, M.R., Collier, R.E.L., Abdul Aziz, L.H., Trout, M., Ferentinos, G., Papatheodorou, G., and Lyberis, E., 2002. Tectono-sedimentary processes along an active marine/lacustrine half-graben margin: Alkyonides Gulf, E. Gulf of Corinth, Greece. *Basin Research*, 14(1):25–41. <https://doi.org/10.1046/j.1365-2117.2002.00164.x>
- Leeder, M.R., Mack, G.H., Brasier, A.T., Parrish, R.R., McIntosh, W.C., Andrews, J.E., and Duermeijer, C.E., 2008. Late-Pliocene timing of Corinth (Greece) rift-margin fault migration. *Earth and Planetary Science Letters*, 274(1–2):132–141. <https://doi.org/10.1016/j.epsl.2008.07.006>
- Leeder, M.R., Mark, D.F., Gawthorpe, R.L., Kranis, H., Loveless, S., Pedentchouk, N., Skourtsos, E., Turner, J., Andrews, J.E., and Stamatakis, M., 2012. A “Great Deepening”: chronology of rift climax, Corinth Rift, Greece. *Geology*, 40(11):999–1002. <https://doi.org/10.1130/G33360.1>
- Leeder, M.R., Portman, C., Andrews, J.E., Collier, R.E.L., Finch, E., Gawthorpe, R.L., McNeill, L.C., Pérez-Arlucea, M., and Rowe, P., 2005. Normal faulting and crustal deformation, Alkyonides Gulf and Perachora Peninsula, eastern Gulf of Corinth Rift, Greece. *Journal of the Geological Society*, 162(3):549–561. <https://doi.org/10.1144/0016-764904-075>
- Lund, S.P., Schwartz, M., Keigwin, L., and Johnson, T., 2005. Deep-sea sediment records of the Laschamp geomagnetic field excursion (~41,000 calendar years before present). *Journal of Geophysical Research: Solid Earth*, 110(B4):B04101. <https://doi.org/10.1029/2003JB002943>
- Lykousis, V., Sakellariou, D., Moretti, I., and Kaberi, H., 2007. Late Quaternary basin evolution of the Gulf of Corinth: sequence stratigraphy, sedimentation, fault-slip and subsidence rates. *Tectonophysics*, 440(1–4):29–51. <https://doi.org/10.1016/j.tecto.2006.11.007>
- Lyons, R.P., Scholz, C.A., Cohen, A.S., King, J.W., Brown, E.T., Ivory, S.J., Johnson, T.C., Deino, A.L., Reinthal, P.N., McCluge, M.M., and Blome, M.W., 2015. Continuous 1.3-million-year record of East African hydroclimate, and implications for patterns of evolution and biodiversity. *Proceedings of the National Academy of Sciences of the United States of America*, 112(51):15568–15573. <https://doi.org/10.1073/pnas.1512864112>
- Manatschal, G., Froitzheim, N., Rubenach, M., and Turrin, B., 2001. The role of detachment faulting in the formation of an ocean-continent transition:

- insights from the Iberia Abyssal Plain. In Wilson, R.C.L., Whitmarsh, R.B., Taylor, B., and Frotzheim, N. (Eds.), *Non-Volcanic Rifting of Continental Margins: A Comparison of Evidence from Land and Sea*. Geological Society Special Publication, 187(1):405–428.
<https://doi.org/10.1144/GSL.SP.2001.187.01.20>
- McHugh, C.M.G., Gungun, D., Giosan, L., Ryan, W.B.F., Mart, Y., Sancar, U., Burckle, L., and Çağatay, M.N., 2008. The last reconnection of the Marmara Sea (Turkey) to the World Ocean: a paleoceanographic and paleoclimatic perspective. *Marine Geology*, 255(1–2):64–82.
<https://doi.org/10.1016/j.margeo.2008.07.005>
- McKenzie, D., 1978. Some remarks on the development of sedimentary basins. *Earth and Planetary Science Letters*, 40(1):25–32.
[https://doi.org/10.1016/0012-821X\(78\)90071-7](https://doi.org/10.1016/0012-821X(78)90071-7)
- McLeod, A.E., Dawers, N.H., and Underhill, J.R., 2000. The propagation and linkage of normal faults: insights from the Strathspey-Brent-Statfjord fault array, northern North Sea. *Basin Research*, 12(3–4):263–284.
<https://doi.org/10.1111/j.1365-2117.2000.00124.x>
- McNeill, L.C., Cotterill, C.J., Henstock, T.J., Bull, J.M., Stafatos, A., Collier, R.E.L., Papatheodorou, G., Ferentinos, G., and Hicks, S.E., 2005. Active faulting within the offshore western Gulf of Corinth, Greece: implications for models of continental rift deformation. *Geology*, 33(4):241–244.
<https://doi.org/10.1130/G21127.1>
- McNeill, L.C., Shillington, D.J., Carter, G., Everest, J., Gawthorpe, R.L., Miller, C.M., Phillips, M., et al., submitted. High resolution record reveals climate-driven environmental and sedimentary changes in an active rift. *Scientific Reports*.
- McNeill, L.C., Shillington, D.J., Carter, G.D.O., Everest, J.D., Le Ber, E., Collier, R.E.L., Cvetkoska, A., De Gelder, G., Diz, P., Doan, M.-L., Ford, M., Gawthorpe, R.L., Geraga, M., Gillespie, J., Hemelsdaël, R., Herrero-Bervera, E., Ismaiel, M., Janikian, L., Kouli, K., Li, S., Machlus, M.L., Maffione, M., Mahoney, C., Michas, G., Miller, C., Nixon, C.W., Oflaz, S.A., Omale, A.P., Panagiotopoulos, K., Pechlivanidou, S., Phillips, M.P., Sauer, S., Seguin, J., Sergiou, S., and Zakharova, N.V., 2019. Expedition 381 facies associations. In McNeill, L.C., Shillington, D.J., Carter, G.D.O., and the Expedition 381 Participants, *Corinth Active Rift Development*. Proceedings of the International Ocean Discovery Program, 381: College Station, TX (International Ocean Discovery Program).
<https://doi.org/10.14379/iodp.proc.381.103.2019>
- Moretti, I., Lykousis, V., Sakellariou, D., Reynaud, J.-Y., Benziane, B., and Prinzhofer, A., 2004. Sedimentation and subsidence rate in the Gulf of Corinth: what we learn from the *Marion Dufresne's* long-piston coring. *Comptes Rendus Geoscience*, 336(4–5):291–299.
<https://doi.org/10.1016/j.crte.2003.11.011>
- Nixon, C.W., McNeill, L.C., Bull, J.M., Bell, R.E., Gawthorpe, R.L., Henstock, T.J., Christodoulou, D., et al., 2016. Rapid spatiotemporal variations in rift structure during development of the Corinth Rift, central Greece. *Tectonics*, 35(5):1225–1248. <https://doi.org/10.1002/2015TC004026>
- Olive, J.-A., Behn, M.D., and Malatesta, L.C., 2014. Modes of extensional faulting controlled by surface processes. *Geophysical Research Letters*, 41(19):6725–6733. <https://doi.org/10.1002/2014GL061507>
- Osmundsen, P.T., and Ebbing, J., 2008. Styles of extension offshore mid-Norway and implications for mechanisms of crustal thinning at passive margins. *Tectonics*, 27(6):TC6016. <https://doi.org/10.1029/2007TC002242>
- Perissoratis, C., Piper, D.J.W., and Lykousis, V., 2000. Alternating marine and lacustrine sedimentation during late Quaternary in the Gulf of Corinth rift basin, central Greece. *Marine Geology*, 167(3–4):391–411.
[https://doi.org/10.1016/S0025-3227\(00\)00038-4](https://doi.org/10.1016/S0025-3227(00)00038-4)
- Rohais, S., Eschard, R., Ford, M., Guillocheau, F., and Moretti, I., 2007. Stratigraphic architecture of the Plio–Pleistocene infill of the Corinth Rift: implications for its structural evolution. *Tectonophysics*, 440(1–4):5–28.
<https://doi.org/10.1016/j.tecto.2006.11.006>
- Rohling, E.J., Marino, G., and Grant, K.M., 2015. Mediterranean climate and oceanography, and the periodic development of anoxic events (sapropels). *Earth-Science Reviews*, 143:62–97.
<https://doi.org/10.1016/j.earscirev.2015.01.008>
- Sachpazi, M., Clément, C., Laigle, M., Hirn, A., and Roussos, N., 2003. Rift structure, evolution, and earthquakes in the Gulf of Corinth, from reflection seismic images. *Earth and Planetary Science Letters*, 216(3):243–257.
[https://doi.org/10.1016/S0012-821X\(03\)00503-X](https://doi.org/10.1016/S0012-821X(03)00503-X)
- Sachpazi, M., Galvé, A., Laigle, M., Hirn, A., Sokos, E., Serpetsidaki, A., Marthelot, J.-M., Pi Alperin, J.M., Zelt, B., and Taylor, B., 2007. Moho topography under central Greece and its compensation by Pn time-terms for the accurate location of hypocenters: the example of the Gulf of Corinth 1995 Aigion earthquake. *Tectonophysics*, 440(1–4):53–65.
<https://doi.org/10.1016/j.tecto.2007.01.009>
- Sadori, L., Koutsodendris, A., Panagiotopoulos, K., Masi, A., Bertini, A., Combourieu-Nebout, N., Francke, A., et al., 2016. Pollen-based paleoenvironmental and paleoclimatic change at Lake Ohrid (south-eastern Europe) during the past 500 ka. *Biogeosciences*, 13(5):1423–1437.
<https://doi.org/10.5194/bg-13-1423-2016>
- Sakellariou, D., and Lykousis, V., 2007. Spatial and temporal evolution of the neotectonic deformation in the Gulf of Corinth [presented at the Geological Society of Greece Symposium in honor of Prof. I. Mariolakis, Athens, Greece, 7 December 2007].
- Sakellariou, D., Lykousis, V., Alexandri, S., Kaberi, H., Rousakis, G., Nomikou, P., Georgiou, P., and Ballas, D., 2007. Faulting, seismic-stratigraphic architecture and Late Quaternary evolution of the Gulf of Alkyonides Basin–East Gulf of Corinth, Central Greece. *Basin Research*, 19(2):273–295.
<https://doi.org/10.1111/j.1365-2117.2007.00322.x>
- Scholz, C.A., Johnson, T.C., Cohen, A.S., King, J.W., Peck, J.A., Overpeck, J.T., Talbot, M.R., et al., 2007. East African megadroughts between 135 and 75 thousand years ago and bearing on early-modern human origins. *Proceedings of the National Academy of Sciences*, 104(42):16416–16421.
<https://doi.org/10.1073/pnas.0703874104>
- Sharp, I.R., Gawthorpe, R.L., Underhill, J.R., and Gupta, S., 2000. Fault-propagation faulting in extensional settings: examples of structural style and synrift sedimentary response from the Suez rift, Sinai, Egypt. *Geological Society of America Bulletin*, 112(12):1877–1899.
[https://doi.org/10.1130/0016-7606\(2000\)112<1877:FPFIES>2.0.CO;2](https://doi.org/10.1130/0016-7606(2000)112<1877:FPFIES>2.0.CO;2)
- Singer, B.S., 2014. A Quaternary geomagnetic instability time scale. *Quaternary Geochronology*, 21:29–52.
<https://doi.org/10.1016/j.quageo.2013.10.003>
- Skourtsos, E., and Kranis, H., 2009. Structure and evolution of the western Corinth Rift, through new field data from the northern Peloponnese. In Ring, U., and Wernicke, B. (Eds.), *Extending a Continent: Architecture, Rheology and Heat Budget*. Geological Society Special Publication, 321(1):119–138. <https://doi.org/10.1144/SP321.6>
- Stafatos, A., Papatheodorou, G., Ferentinos, G., Leeder, M., and Collier, R., 2002. Seismic reflection imaging of active offshore faults in the Gulf of Corinth, Greece: their seismotectonic significance. *Basin Research*, 14(4):487–502. <https://doi.org/10.1046/j.1365-2117.2002.00176.x>
- Stott, L., Poulsen, C., Lund, S., and Thunell, R., 2002. Super ENSO and global climate oscillations at millennial time scales. *Science*, 297(5579):222–226.
<https://doi.org/10.1126/science.1071627>
- Taylor, B., Weiss, J.R., Goodliffe, A.M., Sachpazi, M., Laigle, M., and Hirn, A., 2011. The structures, stratigraphy and evolution of the Gulf of Corinth Rift, Greece. *Geophysical Journal International*, 185(3):1189–1219.
<https://doi.org/10.1111/j.1365-246X.2011.05014.x>
- Taylor, S.K., Bull, J.M., Lamarche, G., and Barnes, P.M., 2004. Normal fault growth and linkage in the Whakatane Graben, New Zealand, during the last 1.3 Myr. *Journal of Geophysical Research: Solid Earth*, 109(B2):B02408.
<https://doi.org/10.1029/2003JB002412>
- Tiberi, C., Lyon-Caen, H., Hatzfeld, D., Achauer, U., Karagianni, E., Kiratzi, A., Louvari, E., et al., 2000. Crustal and upper mantle structure beneath the Corinth Rift (Greece) from a teleseismic tomography study. *Journal of Geophysical Research: Solid Earth*, 105(B12):28159–28171.
<https://doi.org/10.1029/2000JB900216>
- Tzedakis, P.C., Pälike, H., Roucoux, K.H., and de Abreu, L., 2009. Atmospheric methane, southern European vegetation and low–mid latitude links on

- orbital and millennial timescales. *Earth and Planetary Science Letters*, 277(3–4):307–317. <https://doi.org/10.1016/j.epsl.2008.10.027>
- Valet, J.-P., Meynadier, L., and Guyodo, Y., 2005. Geomagnetic dipole strength and reversal rate over the past two million years. *Nature*, 435(7043):802–805. <https://doi.org/10.1038/nature03674>
- Van Avendonk, H.J.A., Lavier, L.L., Shillington, D.J., and Manatschal, G., 2009. Extension of continental crust at the margin of the eastern Grand Banks, Newfoundland. *Tectonophysics*, 468(1–4):131–148. <https://doi.org/10.1016/j.tecto.2008.05.030>
- Whitmarsh, R.B., Manatschal, G., and Minshull, T.A., 2001. Evolution of magma-poor continental margins from rifting to seafloor spreading. *Nature*, 413(6852):150–154. <https://doi.org/10.1038/35093085>
- Zelt, B.C., Taylor, B., Sachpazi, M., and Hirn, A., 2005. Crustal velocity and Moho structure beneath the Gulf of Corinth, Greece. *Geophysical Journal International*, 162(1):257–268. <https://doi.org/10.1111/j.1365-246X.2005.02640.x>
- Zelt, B.C., Taylor, B., Weiss, J.R., Goodliffe, A.M., Sachpazi, M., and Hirn, A., 2004. Streamer tomography velocity models for the Gulf of Corinth and Gulf of Itea, Greece. *Geophysical Journal International*, 159(1):333–346. <https://doi.org/10.1111/j.1365-246X.2004.02388.x>